



## Article

# Landslide Susceptibility Mapping along a Rapidly Uplifting River Valley of the Upper Jinsha River, Southeastern Tibetan Plateau, China

Xiaohui Sun <sup>1,2</sup>, Jianping Chen <sup>2,\*</sup>, Yanrong Li <sup>1</sup> and Ngambua N. Rene <sup>1</sup>

<sup>1</sup> Department of Earth Sciences and Engineering, Taiyuan University of Technology, Taiyuan 030024, China; sunxh17@mails.jlu.edu.cn (X.S.); li.dennis@hotmail.com (Y.L.); lenei0069@link.tyut.edu.cn (N.N.R.)

<sup>2</sup> College of Construction Engineering, Jilin University, Changchun 130026, China

\* Correspondence: chenjp@jlu.edu.cn; Tel.: +86-13843047952

**Abstract:** As a result of the influence of plate movement, the upper reaches of Jinsha River have strong geological tectonic activities, large topographic fluctuations, and complex climate characteristics, which result in the frequent occurrence of landslide disasters. Hence, there is the need to carry out landslide susceptibility mapping in the upper reaches of Jinsha River to ensure the safety of local people's property and the safe exploitation of hydraulic resources. In this study, InSAR technology and a field geological survey were used to map the landslides. Then, the curvature watershed method was used to divide the slope units. A conditioning factor system was established, which can reflect the characteristics of the rapid uplift and vertical distribution of rainfall in the special geological environment of the study area. Finally, logistic regression, random forest, and artificial neural network models were used to establish the landslide susceptibility model. The results show that the random forest model is optimal for the landslide susceptibility mapping in this area. Additionally, the area percentages of the very low, low, moderate, high, and very high susceptibility classes were 40.13%, 20.06%, 13.39%, 12.55%, and 13.87%, respectively. Based on the analysis of the landslide susceptibility map, we suggest that the landslide geological hazards resulting from the rapid uplift of the Tibetan Plateau and the significant decrease in sea level during a glacial period in the upper reaches of Jinsha River are controlled by the double disaster effect of the geodynamic system. Consequently, this study can guide local prevention and mitigation.



**Citation:** Sun, X.; Chen, J.; Li, Y.; Rene, N.N. Landslide Susceptibility Mapping along a Rapidly Uplifting River Valley of the Upper Jinsha River, Southeastern Tibetan Plateau, China. *Remote Sens.* **2022**, *14*, 1730. <https://doi.org/10.3390/rs14071730>

Academic Editors: Chun Zhu, Zhigang Tao, Honghu Zhu, Chen Cao, Manchao He and Michele Saroli

Received: 16 February 2022

Accepted: 1 April 2022

Published: 3 April 2022

**Publisher's Note:** MDPI stays neutral with regard to jurisdictional claims in published maps and institutional affiliations.



**Copyright:** © 2022 by the authors. Licensee MDPI, Basel, Switzerland. This article is an open access article distributed under the terms and conditions of the Creative Commons Attribution (CC BY) license (<https://creativecommons.org/licenses/by/4.0/>).

**Keywords:** landslide susceptibility mapping; Jinsha River; rapidly uplifting; slope unit

## 1. Introduction

A landslide is a natural phenomenon in which slope materials move downward as a result of gravity and other external factors (such as rainfall and earthquakes). The formation process is complex; the sudden outbreak and destructive power are strong [1–6]. It is one of the main threats to the economic and social development in mountainous areas. According to the statistical results in the World Bank (2005) [7], there are  $3.7 \times 10^6$  km<sup>2</sup> of land prone to landslides in the world, and nearly 300 million people live in landslide-prone areas. The economic loss caused by landslides is about USD 20 billion every year. A typical case is the Baige landslide, which collapsed on 10 October and 3 November 2018, in Yunnan Province [8–10], China. More than 3000 houses and more than 3000 hectares of farmland were destroyed, 54,000 people were affected, and economic losses exceeded USD 1.5 billion.

In China, the upper reaches of Jinsha River, which is in the upper reaches of the Yangtze River, have been subjected to the collision and compression of the Pacific and Indian plates for a long time. The terrain has plummeted from northwest to southeast. The river has deep valleys. The new tectonic active faults are widely developed in the region [11], which causes the dynamic regional conditions of high in situ stress and solid seismic activity [12]. Secondly, since the Quaternary, the region has experienced many

glacial periods, resulting in great sea-level changes [13–15]. In addition, this reach has high mountains and deep valleys, and the warm and wet air brought by the monsoon is blocked by the mountains and becomes a dry and hot valley. The precipitation has obvious vertical distribution characteristics [16]. The joint action of internal and external forces creates a special and complex geodynamic environment, characterized by high ground stress, a special internal dynamic environment with strong neo-tectonic and seismic activities, strong unloading in the deep valley, the intense reform of the surface shallow of geological environments, a complex structure of rock mass environment [17–22], complex meteorological hydrological environment, and a special environment of deep overburden [23]. In the special geodynamic environment, the construction of large hydropower stations in the upper reaches of Jinsha River leads to the abnormal development of landslide geological hazards. This also includes the intensification of human engineering activities, which causes the scale to be large, thus resulting in a complex formation mechanism that is, in turn, a significant risk [24,25]. The occurrence of landslides poses a great threat to the safety of life and the property of residents, and the development and utilization of hydropower resources in the area [26–31]. Therefore, research of the landslide hazards and the construction of regional-scale landslide susceptibility mapping method under special geodynamic conditions are an important basis for disaster prevention and reduction research in the upper reaches of Jinsha River. However, the terrain of the study area is steep, and it is difficult to carry out traditional geological disaster monitoring and identification methods, such as borehole inclinometer [32], time domain reflectometry (TDR) [33], optical fiber sensing technology [34], and RGB-D sensors [35], which make it difficult to obtain information about the landslide. Therefore, the construction of reasonable spatial survey means of landslides, to obtain effective information concerning landslide geological disasters, has gradually become a hot issue in geological disaster identification research. With the development of remote sensing technology [36–39] in recent years, the application of this method to landslide identification is gradually increasing, which greatly improves the efficiency of landslide disaster investigations. In addition, there are increasingly more landslide susceptibility models, such as Naïve Bayes [40], decision trees [41], and artificial neural networks [42]. However, the landslide susceptibility model suitable for the special geological environment in the upper reaches of Jinsha River still needs to be explored.

This paper selects the upper reaches of Jinsha River between Xulong village and Benzilan town as the study area. Firstly, based on 3S technology (geographic information system (GIS), the global positioning system (GPS), and remote sensing (RS)) and field investigations, the landslide inventory data are established. Secondly, the curvature watershed method is used to divide the slope units. Based on the analysis of the special environmental characteristics, the conditioning factor system of landslide susceptibility mapping is established following the special geodynamic action of the upper reach of Jinsha River. Then, logistic regression (LR), random forest (RF), and artificial neural network (ANN) models are used to establish the landslide susceptibility model, and statistical parameters and receiver operating characteristic curves are used to optimize the model. Finally, the mapping results are analyzed, and a perspective is presented that suggests that the landslide geological hazards in the upper reaches of Jinsha River are controlled by the double disaster effect of the geodynamic system. This landslide geological hazard is caused by the rapid uplift of the Tibetan Plateau and the great decrease in sea level during the glacial period. The results of this paper can provide guidance for local prevention and mitigation, land planning, and help towards the construction of hydropower stations in the section.

## 2. Study Area

The study area is located upstream of Jinsha River, the junction of the Sichuan and Yunnan provinces (Figure 1a). Because of the uplift of the Tibetan Plateau, the Jinsha River basin is rich in hydropower resources. It has always been a hot area for developing water conservancy and hydropower projects in China. The total length of the studied river stretch is about 100 km, and the flow direction is approximately SSE. The Xulong hydropower

station and Benzilan hydropower station (Figure 1b) are planned to be built on this river reach, with a total hydroelectric generating capacity of 4420 MW.

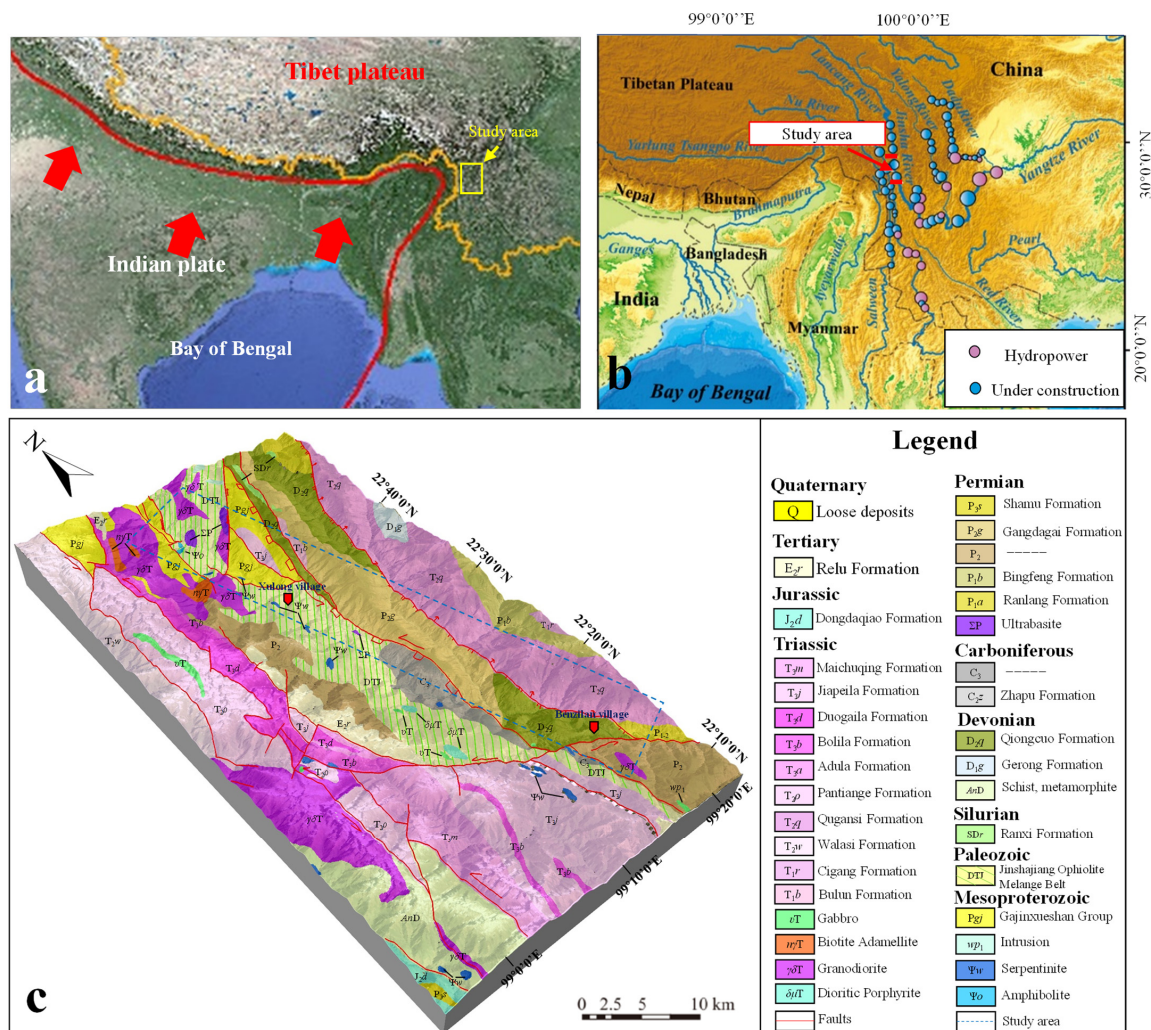


**Figure 1.** The geological and tectonic setting of the study area. (a) The location of the study area, (b) distribution of large hydropower projects in southwest China [11], and (c) geological map of the study area [11].

### 2.1. Topographic Conditions

The study area is located on the southeast margin of the Tibetan Plateau and the northern foothills of the Hengduan Mountains, which is the topographic abrupt change zone of transition from the first step to the second step in China, coupled with the rapid uplift of the Tibetan Plateau and the erosion in Jinsha River [43]. The study area has the characteristics of a high and steep bank slope and a deep valley. On the whole, the mountain elevation in the study area shows a gradually decreasing trend from the northwest to southeast, and the maximum height difference in the area is close to 3000 m. The shape of the river valley is often a “V”, and the bank slope angle is generally greater than 40° [43].

### 2.2. Geologic and Tectonic Settings

Due to the subduction and collision between the Indian and Eurasian Plates, the Tethys Ocean is gradually disappeared during the uplift of the Tibetan Plateau, leaving several plate tectonic sutures, such as the Jinshajiang Suture Zone (JSZ) [11]. The study area is located only in the JSZ (Figure 1c). A strong tectonic movement leads to intense compaction and folding in this area, making the JSZ a weak belt of the Earth’s lithosphere

with extremely endogenic geological activities [11]. The main strata exposed in the study area are shown in Figure 1c. The representative tectonostratigraphic unit of the JSZ is the Jinshajiang Ophiolite Melange Belt (DTJ). As a result of the tectonic activities, the deformation and destruction of rock mass in the DTJ are widespread. In addition, affected by the neotectonic activity, there are several north–south-trending deep and large faults in the study area, such as the Jinshajiang Fault, which led to an Ms 5.9 earthquake on 31 August 2013 near the town of Benzilan.

### 2.3. Climatic Conditions

The study area is located in the subtropical dry-hot valley climate zone. The annual temperature of the study area ranges from 13.8–19.2 °C. The mean annual rainfall is 363.3 mm. Influenced by the latitude, topography, and elevation difference, the climatic characteristics in the study area have significant regional and temporal differences. The regional distribution of the temperature and precipitation in the study area is increasing from upstream to downstream and from west-east to the southwest. In addition, temperature and precipitation also have obvious vertical distribution characteristics [44].

### 2.4. Tectonic Uplift

Due to the subduction and collision between the Indian and Eurasian Plates, the study area has become one of the fastest uplifting regions in the world. Figure 2a summarizes several views on the uplift history of the Tibetan Plateau [11,45,46]. It can be observed that the uplift history of the Tibetan Plateau is controversial. However, scholars of the subject generally believe that the Tibetan Plateau entered a period of rapid uplift in the Quaternary. Xiao and Wang (1998) [47] analyzed and summarized the uplift rate results of the Himalayas and classified the uplift rates belonging to different stages since the Cenozoic Era (Figure 2b). Figure 2b shows that the Tibetan Plateau has entered a rapid–extremely rapid uplift period since the late Pliocene Epoch. The Tibetan Plateau has the fastest uplift rate since the Middle Pleistocene, more than 5 mm/a. Chen and Li (2016) [48] defined the region, with the local crustal uplifting rate greater than 5 mm/a as the rapidly uplifting region and the corresponding river reach as the rapidly uplifting river reach. Therefore, the Jinsha River reach in the study area is a rapidly uplifting river reach.

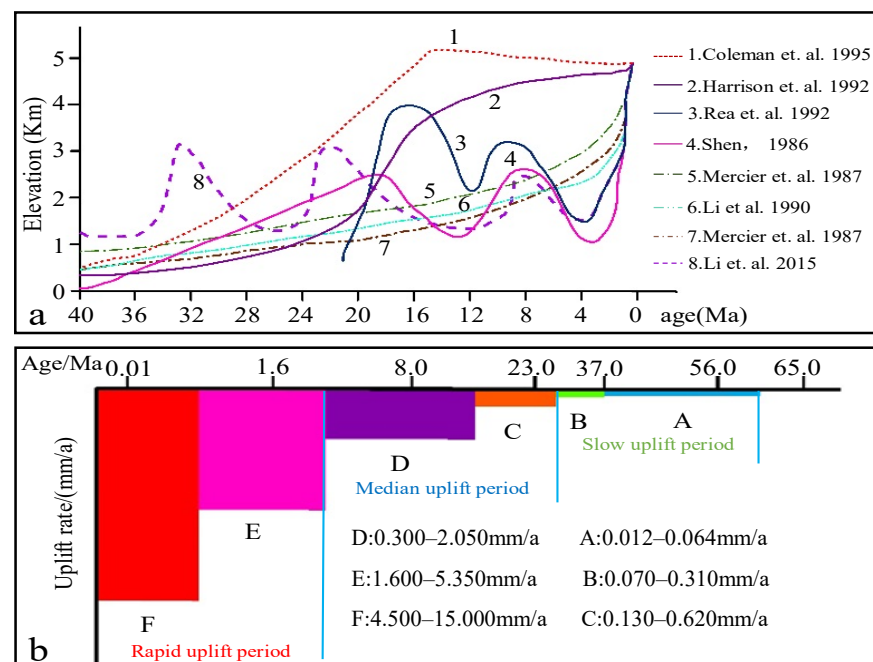


**Figure 2.** (a) Brief summary of the uplift history of the Tibetan Plateau [49], and (b) the uplift rate law of the Tibetan Plateau at different stages since the Cenozoic Era [49].

### 3. Data and Methods

Based on the summary of the relevant scientific papers [50–54], the authors divided the process of landslide susceptibility mapping into the following five parts: (a) landslide inventory data acquisition, (b) mapping unit selection, (c) establishment of conditioning factor system, (d) optimization of the mapping model, and (e) analysis of the mapping results.

#### 3.1. Landslide Characteristics

##### 3.1.1. Landslide Inventory

Landslide inventory data are the basis of the landslide susceptibility mapping [55]. Their detail degree affect the precision of the mapping result. The acquisition of the landslide inventory data was based on a geological field survey. Nowadays, space (e.g., InSAR technology and optical remote sensing technology), air (e.g., airborne radar technology and unmanned aerial vehicle technology), and ground (e.g., ground investigation and geophysical prospecting) technologies are integrated. The geological hazard identification system has been widely used to acquire landslide inventory data [56,57]. To comprehensively and meticulously obtain the landslide inventory data in the study area, a inventory landslide map was produced based on a combination of optical remote sensing interpretation technology, InSAR technology, and field geological surveys (1:100,000). The specific process is as follows:

- (1) According to the characteristics of the landslide and its characteristic marks in optical remote sensing images, the landslides that occurred were interpreted [49]. For example, based on the topographic (Figure 3a) and vegetation (Figure 3b) features of the Yingui landslide in the optical remote sensing image, the Yingui landslide was interpreted.

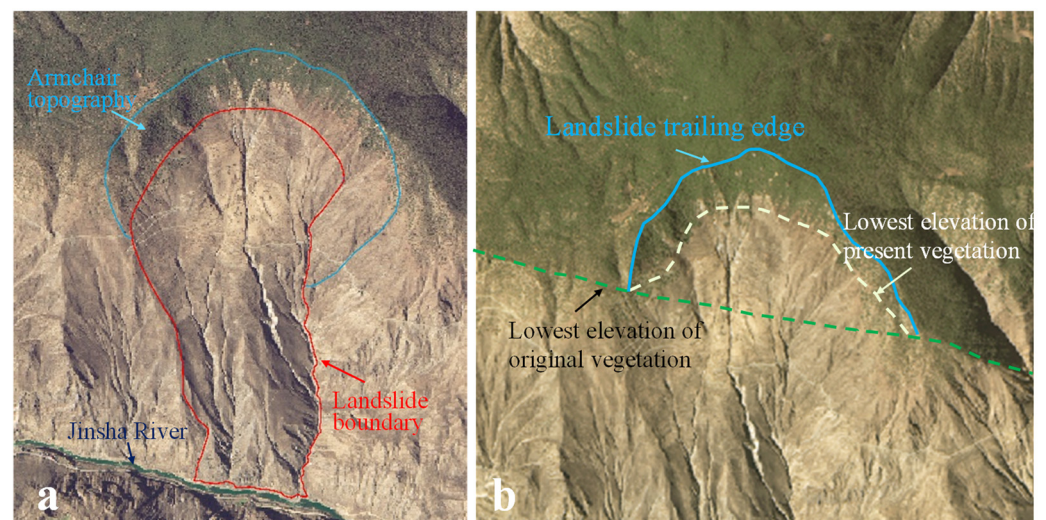


**Figure 3.** Optical remote sensing interpretation mark of the Yingui landslide. (a) topographic features of the Yingui landslide, and (b) vegetation features of the Yingui landslide.

- (2) Based on the monitoring of the surface deformation by InSAR technology, the potential landslides in the deformation stage of the study area that have not been damaged are identified. The study area belongs to the High Mountain and canyon area. Since the SBAS-InSAR technology can improve the coherence of the mountainous area by improving the time sampling rate, this study selected this technology to identify the potential landslide in the study area [58,59]. A total of 23 Sentinel-1A down orbit data with the time period of 12 June 2018–26 May 2019 were used as the InSAR interpretation data. According to the processing process of SBAS-InSAR technology, the connection diagram of the SLC image should be generated first. In this paper, the critical baseline percentage was set as 2, the time baseline was set as 180 days, and

a total of 293 pairs were obtained. Then, the Goldstein method and Minimum Cost Flow method were used to generate the interferogram, and the relativities with a low coherence are removed. Finally, the orbit refining and re-flattening operation, two inversions, and geocoding were carried out to generate the average deformation rate map (Figure 4a). From the average deformation rate diagram of the study area, it can be observed that the deformation rate on both sides of Jinsha River is very high, which is consistent with the distribution law of landslides along the river in the study area. InSAR was based on the interpretation of the landslide study areas, mainly for clustering the deformation rate of the large area, using the Taentong landslide as an example. Although the landslide that is based on optical remote sensing is visible, there is a high concentration of the deformation zone when the interpretation based on InSAR technology is found in the Taentong landslide in zone II (Figure 4b). Therefore, it is speculated that the Taentong landslide in this area may present signs suggesting that it might reoccur.

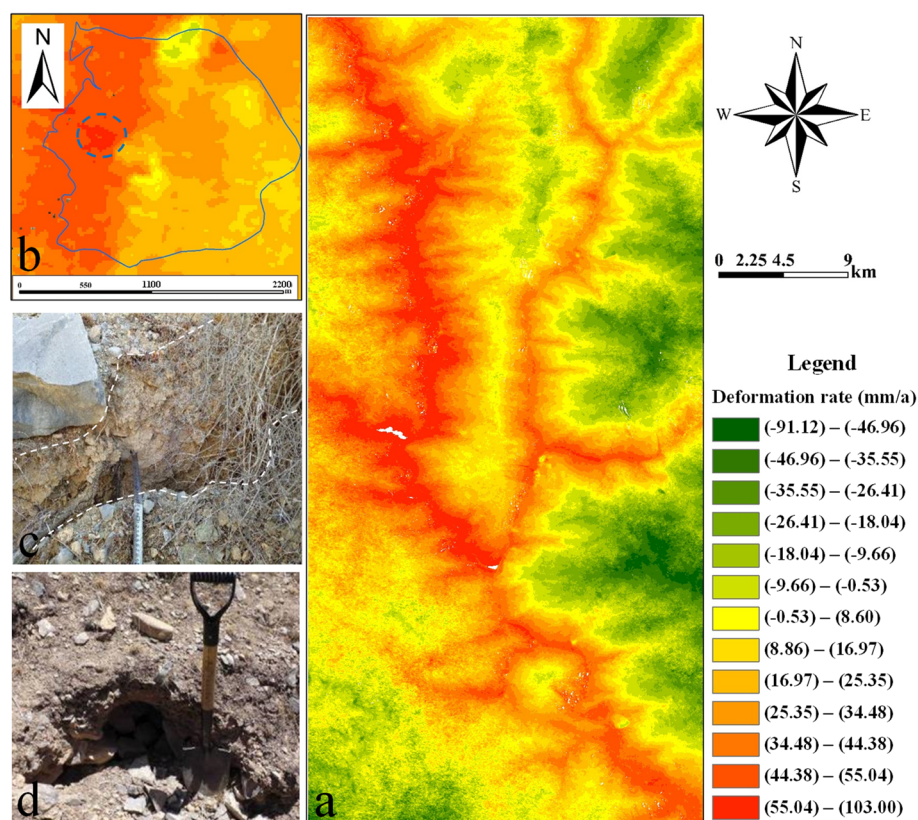


**Figure 4.** (a) InSAR interpretation results of the study area, and (b–d) InSAR interpretation results of the Taentong landslide and its internal tensile cracks.

- (3) Based on the field investigation, the interpretation results are checked and the uninterpreted landslides are supplemented [60]. For example, through the field investigation, the interpretation results of the Taentong landslide were verified. The developing tensile crack was found in the inner part of the Taentong landslide, which showed that the Taentong landslide underwent deformation (Figure 4c,d).

Based on the above methods, a total of 61 landslides were mapped in the study area. The maximum area of the landslides is  $392.0 \times 10^4 \text{ m}^2$ , the minimum area of the landslides is  $1.6 \times 10^4 \text{ m}^2$ , and the mean area of the landslides is  $63.69 \times 10^4 \text{ m}^2$ . Additionally, its distribution characteristics are shown in Figure 5.

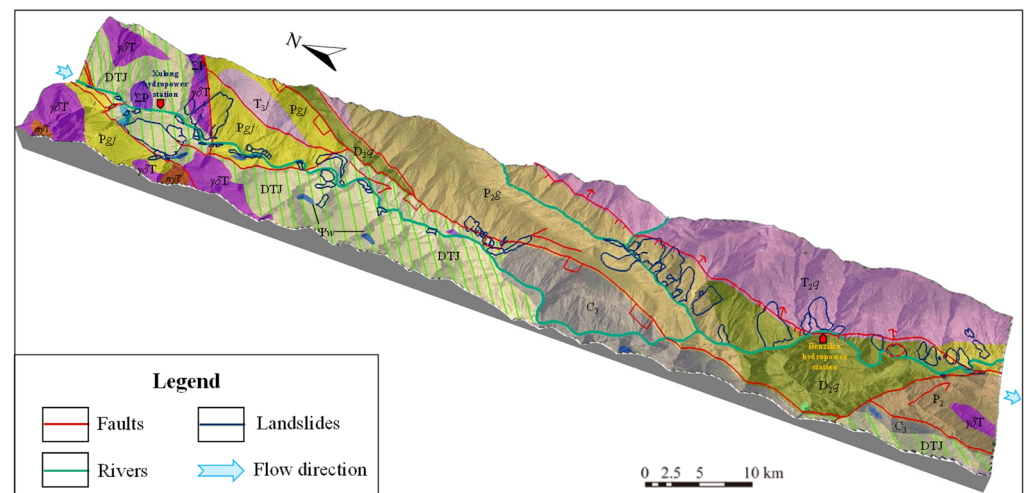


**Figure 5.** Landslide inventory data map and typical landslides in the study area.

### 3.1.2. Spatial Distribution of the Landslides

Based on Figure 5, it can be observed that the landslides in the study area have obvious linear distribution and aggregation distribution characteristics.

- (1) Linear distribution characteristics: landslides in the study area are mainly distributed along the two banks of Jinsha River and its tributary, Dingqu River, in the north–south direction.
- (2) Clustering distribution characteristics: landslides in the study area are mainly concentrated in Xulong–Maoding (13), Qulong–Rongxue (15), Guxue–Rancun (14), and Quzhi–Yahong (14), indicating that the distribution of the landslides is concentrated and the clustering is strong.

### 3.1.3. Landslide Mechanism

According to the field investigation, the main lithologies exposed in the study area are lamellar greenschist and lamellar slate. Under the continuous action of the Eurasian Plate and the Asian Plate, according to history, these rocks suffered from the maximum principal stress in the near east and west directions. They formed nearly vertical, steeply dipping lamellar rocks parallel to the north–south rivers. Due to the tectonic stress, joints and fissures developed in the rock mass. As a result of this, the landslides in the study area are mainly of the bending-cracking (39) and creep-cracking types (13). Additionally, there are a small number of slip-bending, slip-tension, and slip-pressure-induced fracture types, which are 5, 3, and 1, respectively.

### 3.2. Mapping Units

The mapping unit is the basic unit of landslide susceptibility mapping. It has the characteristics of homogeneity within units and heterogeneity among units. It is also the smallest and indivisible basic unit in landslide susceptibility mapping. Common mapping units mainly include a grid unit, watershed unit, slope unit, regional unit, and uniform condition unit [49,61]. The slope unit is closely related to the real topography unit. It can reflect the difference between topography and geology [49], which is extensively used in landslide susceptibility mapping. The division methods of slope units are becoming more and more diverse. By summarizing the current division methods, Wang et al. (2020) [62] determined four commonly used division methods of slope units: the hydrological analysis method, curvature watershed method, r.slopeunits method [63], and MIA-HUS method. Among them, the hydrologic analysis and curvature watershed methods are simple and easy to implement. In this paper, priority is given to using these two methods to divide the slope units. By comparing the effects of these two methods, Sun et al. [49] found that the slope units divided by the curvature watershed method were more concentrated in the

area, more regular in shape, more uniform in the interior, and less work was needed for manual modification. Therefore, the curvature watershed method is finally used in this paper to divide the slope units in the study area. The specific process of dividing the slope units by the curvature watershed method is shown in Figure 6.

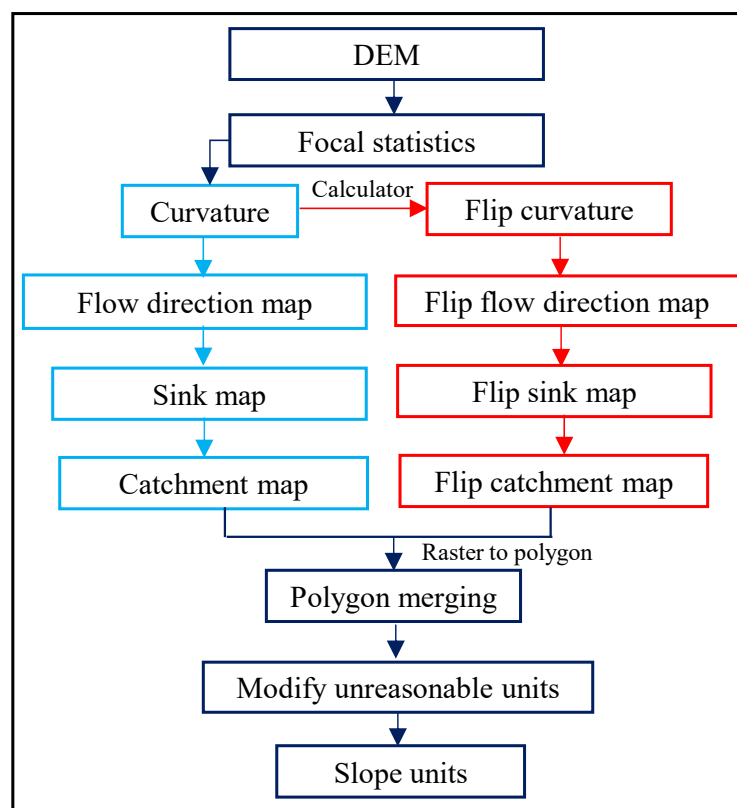


**Figure 6.** Slope unit division flowchart.

### 3.3. Conditioning Factors

#### 3.3.1. Establishment of the Conditioning Factor System

Nowadays, the selection of conditioning factors mostly depends on the field investigation cause analysis, expert experience, and relevant literature. The factors with the highest correlation to the occurrence of landslides are selected. Pourghasemi and Rossi (2017) [64] performed a statistical analysis on the frequency of the commonly used conditioning factors from 220 pieces of relevant literature published from 2005 to 2012 in different ISI journals (International Scientific Indexing). The results showed the most frequently used slope angle, lithology, slope aspect, land use, distance from the river, elevation, distance from the faults, plan curvature, profile curvature, and distance from road (top ten).

Additionally, the authors analyzed the geological environment of the study area. The study area is located in the southeastern margin of the Tibetan Plateau. Due to the plate tectonic movement, the geological conditions in the area are complex, which can be reflected in the following aspects:

- (1) The rock mass structure is complex

A variety of lithologies are exposed in the study area, and the contact relationship between them is complex. As shown in Figure 7a, the irregular contact relationship of diorite, gneiss, and green schist in the Xulong valley outlet constitutes the characterization of the complex structural rock mass in the study area. In addition, the deformation characteristics of the rock mass are also very significant.

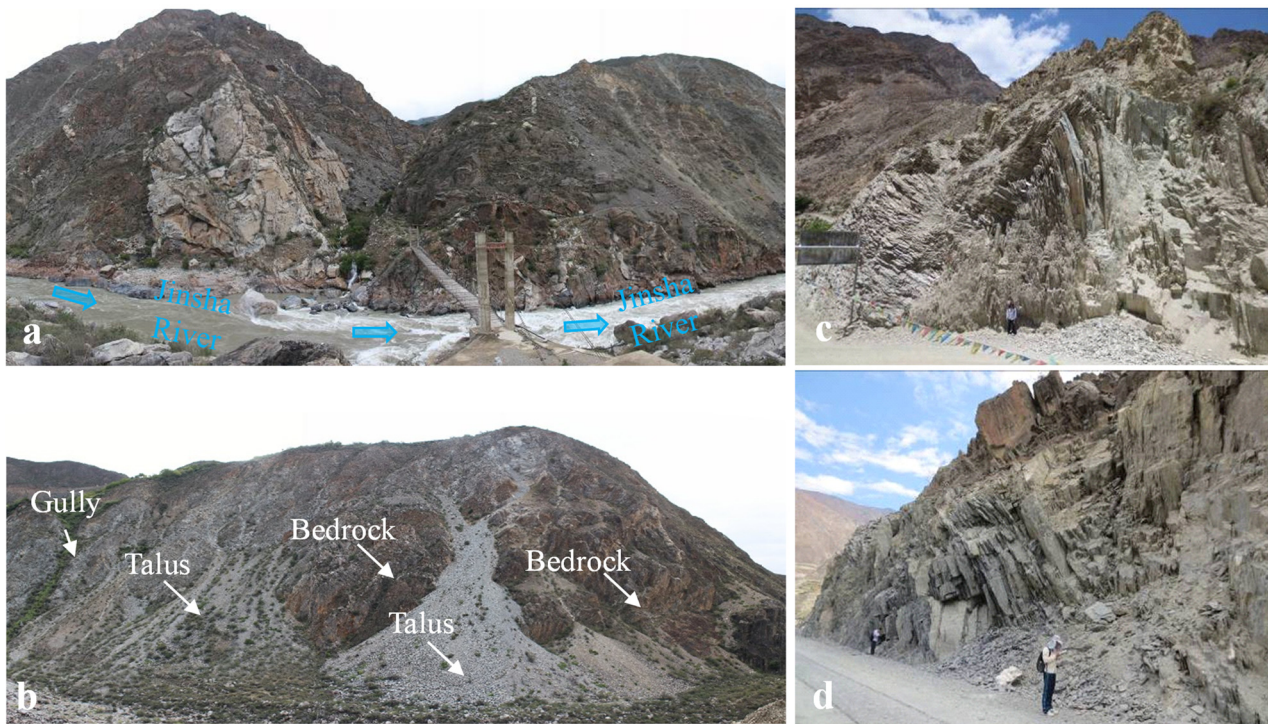


**Figure 7.** The rock mass structure characteristics and topographic characteristics of the study area, and the deformation characteristics of the rock mass in the study area. (a) Rock mass structure characteristics, (b) topographic characteristics, and (c,d) the deformation characteristics of the rock mass.

(2) The topographic characteristics are complex

The study area is located in the topographic abrupt change zone of transition from the first to the second step in China. It has been subjected to the uplift of the Tibetan Plateau and the erosion in Jinsha River over a long period of time, so the study area has the characteristics of a high and steep bank slope and deep valley [44]. In addition, due to the historical glaciation, there are many glacial erosion landforms in the study area, followed by landslide residual landforms, river erosion landforms, and other landforms. For example, in addition to the rock mass and weathered layer, different sediments or deposits exist in different parts of the left bank slope in the lower reaches of Xulong Valley (Figure 7b).

(3) The geological structure is complex

Due to the location of the study area, it has been subjected to the continuous action of two large plates (India Plate and Eurasian Plate) over a long period of time, and the tectonic activities in the area are powerful. Under the tectonic activities, the deformation and destruction of rock mass are pervasive (Figure 7c,d). There are several large faults in the study area, which greatly affect the stability of the slope.

(4) The climatic characteristics are complex

Influenced by the elevation and monsoon of the Tibetan Plateau, the climate characteristics in the region are complex. In addition to the increasing trend from upstream to downstream, the temperature and rainfall in the region also have obvious vertical distribution characteristics [65]. In the field investigation, it was found that many loose deposits in the study area could be stably preserved on both sides of the river, for which it is difficult to survive under the normal rainfall conditions in mountainous areas. This phenomenon is the influence of the vertical distribution characteristics of rainfall in the study area.

To summarize, when selecting conditioning factors, the geological factors of the study area should be fully considered, such as the lithology and faults, followed by the topographic factors, such as the slope angle and elevation. Thirdly, it is necessary to integrate the

vertical climate characteristics and crustal uplift rate with the above traditional geological factors to establish a conditioning factor system that is more in line with the geological characteristics of the study area. Therefore, this paper establishes the conditioning factor system as shown in Table 1. The data sources of each conditioning factor extraction and the mutator methods of each conditioning factor to the slope unit are listed in Table 1. The conditioning factors are shown in Figure 8.

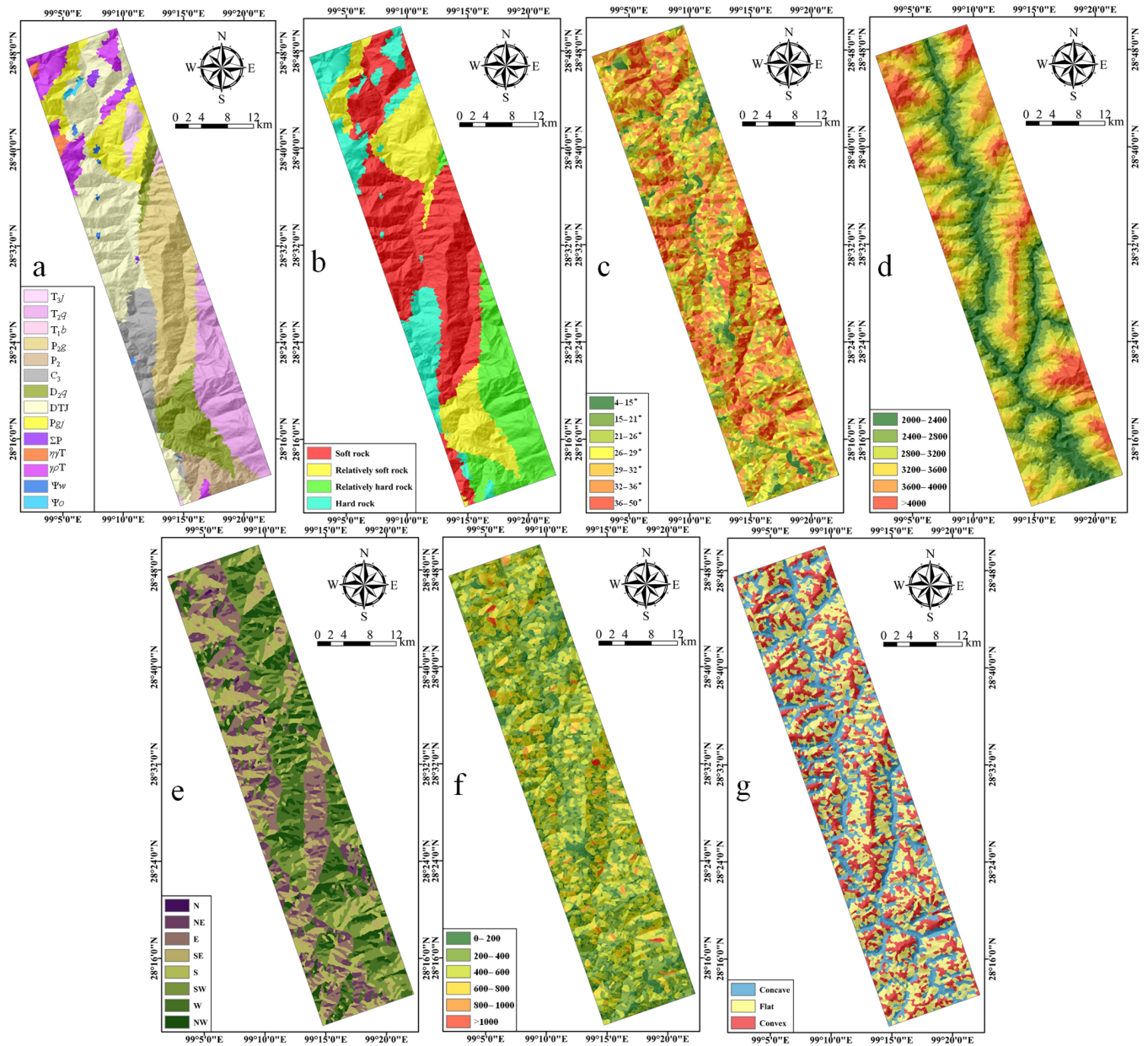
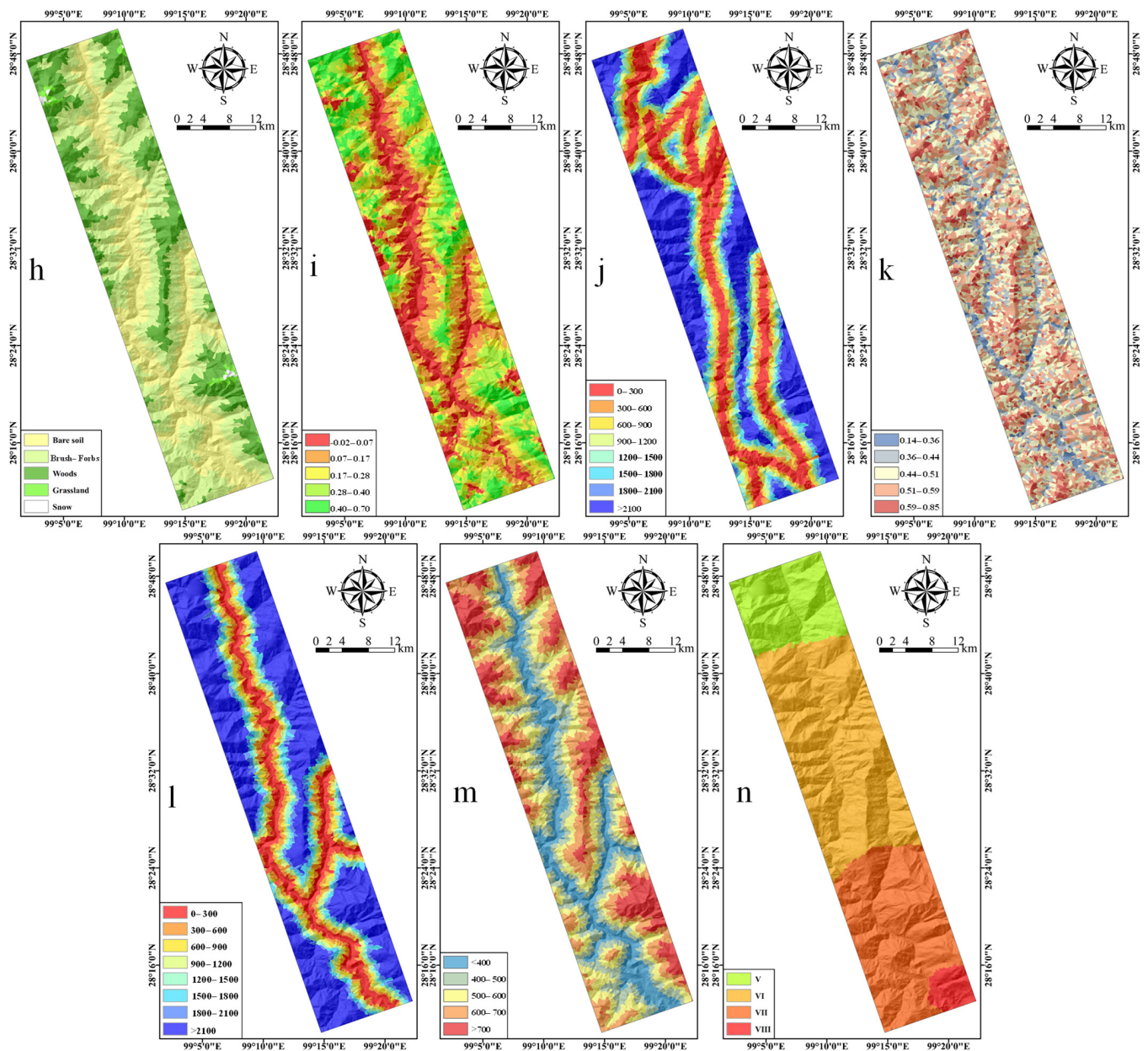


Figure 8. Cont.



**Figure 8.** Landslide conditioning factor maps: (a) lithology; (b) rock hardness; (c) elevation; (d) slope angle; (e) slope aspect; (f) topographic relief; (g) curvature; (h) land use; (i) normalized difference vegetation index (NDVI); (j) distance from faults; (k) Strahler's integral value; (l) distance from rivers; (m) rainfall; and (n) earthquake intensity.

### 3.3.2. Multicollinearity Analysis of the Conditioning Factors

Many landslide susceptibility models, such as the logistic regression model, are susceptible to the multicollinearity of conditioning factors. Therefore, it is necessary to eliminate the multicollinearity among the conditioning factors before modeling. The Principal Component Analysis (PCA) uses a small number of principal components to represent the original evaluation index system, eliminating the problem of multicollinearity among the conditioning factors and resulting in a small loss of information from the original conditioning factors [44]. Therefore, in the present paper, PCA is selected to eliminate the multicollinearity among the evaluation indexes. Before the PCA, the following equation is used to normalize the conditioning factors to eliminate the dimensional influence:

$$M = (H - H_{min}) / (H_{max} - H_{min}), \quad (1)$$

where  $M$  is the normalized conditioning factors;  $H$  is the conditioning factors; and  $H_{min}$  and  $H_{max}$  are the minimum and maximum values of the conditioning factors, respectively.

**Table 1.** Landslide conditioning factors in the present study.

Conditioning Factors	Data Source	Variable Type	Mutator Methods of the Slope Units
Lithology	Department of Geological Survey (1:200,000 scale)	Categorical	Major value
Rock hardness		Categorical	Major value
Elevation	Digital elevation model (91 Weitu software, 8.96 m)	Continues	Average value
Slope angle		Continues	Average value
Slope aspect		Continues	Average value
Topographic relief		Continues	Average value
Curvature		Continues	Average value
Land use		Landsat 5 TM images (3 April 2015)	Categorical
NDVI	Continues		Average value
Distance from faults	Department of Geological Survey (1:200,000 scale)	Continues	Average value
Strahler's integral value	Sun et al., 2020c	Continues	Average value
Distance from rivers	Department of Geological Survey (1:200,000 scale)	Continues	Average value
Rainfall	Sun et al., 2019 [65]	Continues	Average value
Earthquake intensity	Lai et al., 2014 [66]	Categorical	Major value

### 3.4. Landslide Susceptibility Models

#### 3.4.1. Logistic Regression Model

The logical regression (LR) model has very low requirements for data types, and the data can either be continuous or discrete. Therefore, it is one of the nonlinear evaluation methods widely used for landslide susceptibility mapping [67–70]. This model represents landslide occurrence in a binary form (1 represents “landslide” and 0 represents “non-landslide”). The conditioning factors are converted into logical variables to determine the possibility of landslides in the future. The LR model can be expressed as follows [44]:

$$P = 1/(1 + e^{-z}), \quad (2)$$

where  $P$  is the susceptibility index of landslide occurrence and  $z$  is the weighted sum of each conditioning factor, which can be expressed as follows:

$$z = \beta_0 + \beta_1 Y_1 + \beta_2 Y_2 \dots + \beta_G Y_G, \quad (3)$$

where  $\beta_0$  is the constant term;  $\beta_1, \beta_2 \dots \beta_G$  are the logistic regression coefficients; and  $Y_1, Y_2 \dots Y_G$  are the conditioning factors.

#### 3.4.2. Random Forest Model

The random forest (RF) model consists of multiple decision trees [71]. The original data set is extracted into multiple subsamples by random sampling with put back, and then the decision tree is used to model each subsample. Finally, all the models are combined and the best model is selected by voting. This model adopts random sampling, which can prevent the over-fitting of the model. In addition, it has a high tolerance to outliers and has become one of the most commonly used and high-precision machine learning methods for landslide susceptibility mapping [72–75].

#### 3.4.3. Artificial Neural Network Model

A complete artificial neural network (ANN) model usually consists of one input layer, one or more hidden layers, and one output layer. Each layer is made up of multiple neurons. The ANN model completes the entire learning process by adjusting the weight

value between each neuron. The ANN model is simple and has quick solving and learning abilities, so it is also widely used for landslide susceptibility mapping [76–78].

### 3.5. Validation and Comparison Methods

#### 3.5.1. K-Fold Cross-Validation

K-fold cross-validation can overcome the problem of insufficient data and over-fitting in the process of modeling. In this paper, the landslide susceptibility model was validated by using the method of five-fold cross-validation [43,49]. The basic principles are as follows:

- (1) The data were randomly divided into five subsets.
- (2) Four subsets were used to build the landslide susceptibility model, and the other subset was used as the test datum.
- (3) Steps 1–2 were repeated until all five subsets were used as the training data and test data, respectively. In this way, a total of five models were established and five validations were carried out.
- (4) The prediction accuracy of the five-times modeling was incorporated, and the prediction accuracy of the different landslide susceptibility models was evaluated.

#### 3.5.2. Statistical Analysis Method

The accuracy, sensitivity, specificity, positive predictive value, and negative predictive value can be used to evaluate the effectiveness of the landslide susceptibility model prediction [43], which the following formula can calculate:

$$AC = \text{Accuracy} = (TP + TN)/(TP + TN + FP + FN); \quad (4)$$

$$SE = \text{Sensitivity} = TP/(TP + FN); \quad (5)$$

$$SP = \text{Specificity} = TN/(TN + FP); \quad (6)$$

$$PPV = \text{Positive predictive value} = TP/(TP + FP); \quad (7)$$

$$NPV = \text{Negative predictive value} = TN/(TN + FN); \quad (8)$$

where TP is the true positive; TN is the true negative; FP is the false positive; and FN is the false negative.

#### 3.5.3. Receiver Operating Characteristic Curve

The receiver worker characteristic curve (ROC) is the most commonly used quantitative evaluation method for the prediction accuracy of the landslide susceptibility model [16,43]. The curve of the ROC was drawn with the false positive rate (sensitivity) as the  $x$ -axis, the true positive rate (1-specificity) as the  $y$ -axis, and the area under the curve was the value of the AUC. The AUC value is between 0.5 and 1, and the greater the value, the higher the model's prediction accuracy.

### 3.6. Photoluminescence Dating Analysis of the Occurrence Date of the Landslides

In the present study, photoluminescence dating analysis was conducted to roughly determine the occurrence date of the landslides. After the material is covered by the upper material, it is not affected by light and can only receive the cosmic radiation emitted by the decay of the radioactive material in its environment. After absorbing this radiation, the crystal electrons inside the slippery material ionize and produce free electrons as a result of absorbing energy. These electrons are stored as "trapped electrons" in the lattice and, as time goes by, the number of "trapped electrons" in the lattice increases, which is equivalent to storing the energy of the cosmic radiation it receives. When this stored radiation energy is exposed to light or heated, it is released, producing an optical signal. The amount of luminescent signal that can be released in a substance is proportional to the total amount of radiation received. Additionally, their radiation exposure increases over time, so that its age can be measured [79]. To determine the landslides occurrence date, the sliding

zone soil was selected to determine the age of the landslide occurrence in a completely shaded environment.

## 4. Results

### 4.1. Slope Unit Division Results

It can be observed in Figure 6 that the division accuracy of the curvature watershed method is affected by the resolution of the digital elevation model (DEM). In this paper, a DEM with a resolution of 8.96 m was downloaded from the 91 Weitu software (GoogleEarth DEM) to divide the slope units. To find the most reasonable division results, the resolution of the DEM data was converted into 5.0 m, 10.0 m, 30.0 m, 50 m, 80.0 m, 100.0 m, and 120.0 m for the slope unit divisions. By comparing the division results under different resolutions with the Ziyuan-3 satellite image, it was found that when the resolution of the DEM is 100.0 m, the divided slope units were most consistent with the real terrain in the study area. The study area is divided into 5421 units, of which the most significant unit is 1.048 km<sup>2</sup>, and the smallest unit is 0.001 km<sup>2</sup> (Figure 9a).

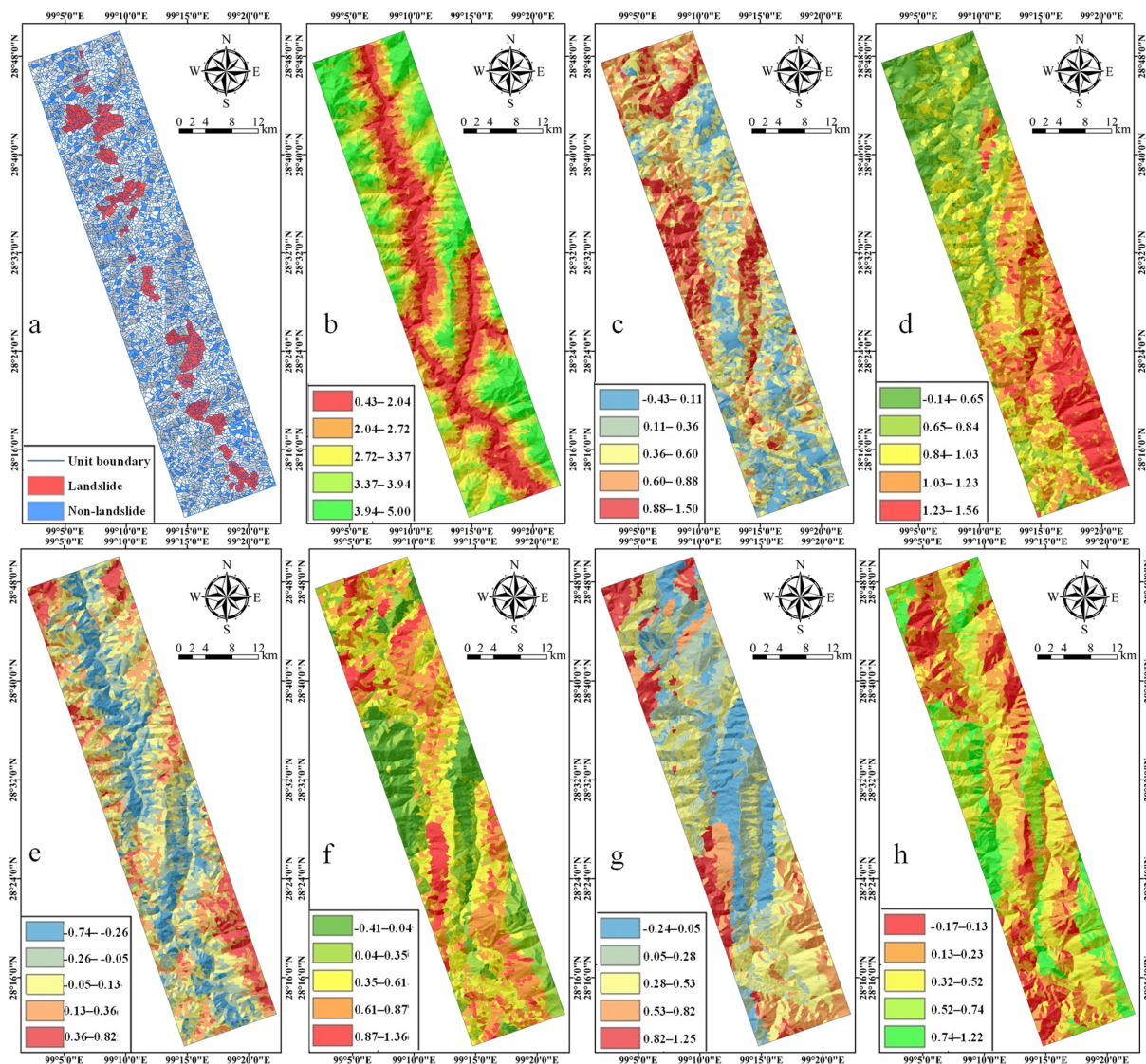


**Figure 9.** The results of the slope unit division and principal component extraction. (a) Slope unit division result; (b) principal component 1; (c) principal component 2; (d) principal component 3; (e) principal component 4; (f) principal component 5; (g) principal component 6; and (h) principal component 7.

#### 4.2. Multicollinearity Analysis Results

The Kaiser–Meyer–Olkin (KMO) and Bartlett’s tests are used to test whether the conditioning factors system is suitable for principal component analysis. From Table 2, it can be observed that the KMO value of the conditioning factors system is 0.764, greater than 0.750, which indicates that the multicollinearity among the conditioning factors is large and a principal component analysis should be conducted. By calculating the maximum eigen roots of the correlation matrix, the eigen roots greater than 0.75 are selected as the main components. It can be observed from Table 3 that 7 principal components were selected, and the cumulative sum of the variance of these 7 principal components was greater than 80%, indicating that more than 80% of the original conditioning factors’ information was retained. The extraction results of the seven principal components are shown in Figure 9b–h.

**Table 2.** Results of the KMO and Bartlett’s tests.

KMO test	0.764
Bartlett’s test	48,271.116
<i>p</i> -value	0.000

**Table 3.** Total variance explained.

Components	Initial Eigenvalues			Extraction Sums of Squared Loadings		
	Total	% of Variance	Cumulative %	Total	% of Variance	Cumulative %
1	4.517	32.263	32.263	4.517	32.263	32.263
2	1.769	12.634	44.897	1.769	12.634	44.897
3	1.532	10.940	55.837	1.532	10.940	55.837
4	1.231	8.795	64.632	1.231	8.795	64.632
5	1.074	7.670	72.302	1.074	7.670	72.302
6	0.977	6.977	79.279	0.977	6.977	79.279
7	0.759	5.422	84.702	0.759	5.422	84.702
8	0.560	3.999	88.700	-	-	-
9	0.468	3.346	92.046	-	-	-
10	0.413	2.953	94.999	-	-	-
11	0.348	2.484	97.483	-	-	-
12	0.256	1.831	99.314	-	-	-
13	0.082	0.585	99.899	-	-	-
14	0.014	0.101	100.000	-	-	-

#### 4.3. Model Fitting Results

The seven principal components obtained by the PCA were introduced to establish the LR, RF, and ANN models. The establishment of the landslide susceptibility model requires an equal number of landslide and non-landslide units to participate in the modeling [49]. Firstly, based on the division results of the slope units and landslide inventory map, it was determined that there were 575 landslide units in the study area. Then, to meet the modeling requirements, the non-landslide units equal to the number of landslide units were randomly selected in a place that was at least 200 m away from the landslide units. Finally, the data were divided into five equal parts using five-fold cross-validation. All models were established in IBM SPSS software. For the LR model, all the principal components were entered into the model, and the significance level was set at 95% [43]. As for the RF model, the number of decision trees constructed was 300, the sample size was 1.0, and the unbalanced data were processed. Set the maximum number of nodes in the tree to 10,000, the maximum depth to 10, and the minimum child node size to 5 [80]. The ANN model consists of an input layer, a hidden layer, and an output layer. The activation function was set as a logistic sigmoid. The momentum, learning rate, and training time were set as 0.3, 0.3, and 500, respectively [81]. The results are shown in Table 4.

**Table 4.** The performances for the two slope units' fitted landslide susceptibility models (%).

Method	Index	Training							Validating						
		K = 1	K = 2	K = 3	K = 4	K = 5	Mean	Standard Deviation	K = 1	K = 2	K = 3	K = 4	K = 5	Mean	Standard Deviation
LR	AC	0.782	0.775	0.786	0.777	0.778	0.780	0.004	0.765	0.800	0.743	0.778	0.778	0.773	0.021
	SE	0.769	0.761	0.773	0.766	0.768	0.767	0.005	0.780	0.785	0.737	0.746	0.781	0.766	0.022
	SP	0.795	0.791	0.800	0.789	0.790	0.793	0.004	0.752	0.817	0.750	0.820	0.776	0.783	0.034
	PPV	0.804	0.802	0.809	0.798	0.798	0.802	0.005	0.739	0.826	0.757	0.843	0.774	0.788	0.045
	NPV	0.759	0.748	0.763	0.757	0.759	0.757	0.006	0.791	0.774	0.730	0.713	0.783	0.758	0.034
	AUC	0.856	0.856	0.863	0.859	0.853	0.857	0.003	0.861	0.856	0.829	0.843	0.873	0.852	0.015
RF	AC	0.898	0.911	0.903	0.889	0.887	0.898	0.010	0.804	0.804	0.817	0.830	0.817	0.815	0.011
	SE	0.880	0.900	0.894	0.907	0.874	0.891	0.014	0.843	0.802	0.823	0.806	0.817	0.818	0.016
	SP	0.918	0.922	0.913	0.873	0.901	0.905	0.020	0.773	0.807	0.812	0.858	0.817	0.814	0.030
	PPV	0.922	0.924	0.915	0.867	0.904	0.907	0.023	0.748	0.809	0.809	0.870	0.817	0.810	0.043
	NPV	0.874	0.898	0.891	0.911	0.870	0.889	0.017	0.861	0.800	0.826	0.791	0.817	0.819	0.027
	AUC	0.964	0.968	0.965	0.963	0.962	0.964	0.002	0.849	0.881	0.871	0.878	0.869	0.870	0.011
ANN	AC	0.822	0.853	0.863	0.841	0.832	0.842	0.017	0.804	0.787	0.783	0.796	0.791	0.792	0.008
	SE	0.826	0.842	0.846	0.828	0.827	0.834	0.010	0.843	0.770	0.773	0.779	0.786	0.790	0.030
	SP	0.818	0.865	0.881	0.855	0.837	0.851	0.025	0.773	0.806	0.793	0.815	0.796	0.797	0.016
	PPV	0.815	0.870	0.887	0.861	0.839	0.854	0.028	0.748	0.817	0.800	0.826	0.800	0.798	0.030
	NPV	0.828	0.837	0.839	0.822	0.824	0.830	0.008	0.861	0.757	0.765	0.765	0.783	0.786	0.043
	AUC	0.891	0.921	0.926	0.908	0.906	0.910	0.012	0.891	0.884	0.883	0.897	0.896	0.890	0.006

## 5. Discussion

### 5.1. Model Comparison

The confusion matrix was obtained through the training and testing of the three models. The corresponding statistical parameters of each model were calculated to evaluate the advantages and disadvantages of each model. Table 4 shows that in the training stage, the mean accuracy of the RF model is 0.898, which is higher than that of the other two models, followed by the ANN model (0.842) and LR model (0.780). In the test stage, the mean accuracy of the RF model was also the highest. The accuracy of the ANN model was very close to the RF model, with a difference of 0.023, indicating that the mean accuracy of the two models in the test stage was the same. As for the standard deviation of the mean accuracy, the LR model had the smallest standard deviation in the training stage, indicating that it was the most stable model, followed by the RF model and the ANN model. In the test stage, the accuracy standard deviation of both the LR and the RF models increased, but the ANN model decreased, indicating that the ANN model had good stability in the test stage. In terms of accuracy, the average accuracy and the standard deviation of all three models decreased in the test stage, in comparison to the training stage. However, the decrease was not significant, and the accuracy standard deviation was below 0.02. Therefore, the RF model is considered as the optimal model, only from the perspective of accuracy. For the other four statistical parameters, the standard deviations were small, only in the LR model during the training stage. For the RF and ANN models, the standard deviations of these four statistical parameters were all large, indicating that the stability of the two models decreased.

Moreover, the standard deviations of the four statistical parameters in the test stage significantly increased, compared to the training stage, indicating that the stability of the three models in the test stage was worse than that in the training stage. According to the mean value of the four statistical parameters, the RF model was significantly higher than the other two models in the training stage. According to the average value of the four statistical parameters, the RF model was superior to the ANN model, and the ANN model was superior to the LR model. Although there were slight differences in the four statistical parameters between the ANN and RF models in the test stage, the difference was insignificant. The maximum difference was below 0.035, indicating that the two models had the same prediction effect on the landslide and non-landslide units in the test stage.

In summary, among the landslide susceptibility models established by the three models, the LR model is the most stable in the training stage, which means that the standard deviations of its five statistical parameters are all small. In the test stage, the stability of the three models decreases to varying degrees. The most stable model is the LR model, in terms of the standard deviation ranking, while the stability difference between the RF and ANN models is not significant. For the mean value of the five statistical parameters, the RF model is higher than the ANN model in the training stage, and the LR model is the lowest. The LR model is also the lowest in the test stage, but there is little difference between the RF and ANN models. Therefore, by comparing the five statistical parameters, out of the above-mentioned three models, the RF model can be regarded as the most reasonable model.

Through the training and testing of the three models, the ROC curve was obtained, and the AUC value was calculated. Table 4 reveals that the mean AUC value of the LR model is 0.857 in the training stage and 0.852 in the test stage; the mean AUC value of the RF model is 0.960 in the training stage and 0.870 in the test stage; and the mean AUC value of the ANN model is 0.910 in the training stage and 0.890 in the test stage. As for the standard deviation of the AUC value, the ANN and LR models are larger than the RF model, smaller, and have better stability. From the perspective of the AUC value, the RF model is also the most reasonable model out of the above-mentioned three models.

### 5.2. Model Comparison with Other Studies

Some studies were conducted in a similar area. Cao et al. (2016) [23] analyzed the landslide susceptibility of the Xulong Reservoir, by using a combination of the information content method and the analytic hierarchy process, and using the grid units as the mapping units. In the present study, the authors innovatively quantified the vertical rainfall characteristics in the study area. It is indicated that the vertical rainfall characteristics are one of the geological environment factors that should be specially considered in the landslide susceptibility of the study area. Based on the research of Cao et al., Sun et al. (2018) [44] used the frequency ratio (FR), analytic hierarchy process (AHP), logistic regression (LR), and principal component analysis (PCA) to study the landslide susceptibility in Derong County and Deqin County in the upper reaches of Jinsha River. This study also considered the vertical rainfall characteristics in the study area, and the represented river incision and bedrock uplift by slope angle. Their study verified the main reasons for the occurrence of landslides along the river in the study area. Sun et al. (2020) [43] used slope units divided by the hydrologic method to study the susceptibility of landslides in the upper Jinsha River and innovatively used the Straliet integral value to characterize the bedrock uplift in the study area. It can be observed from Table 5 that the prediction accuracy of this study is much higher than that of Cao et al. (2016) [23] and Sun et al. (2018) [44], and the main difference between them is the difference of the mapping units. This is because the slope unit is more closely related to the geological and geomorphological characteristics. Sun et al. (2020) [49] found that the slope unit divided by the curvature watershed method has a uniform size, shape between the circle and equilateral triangle, and small internal terrain. Based on the above research, this study hopes to establish a landslide susceptibility mapping method more suitable for the special geological environment characteristics of the upper Jinsha River. Based on the analysis of the geological environment in the study area, the present paper establishes a landslide susceptibility conditioning factor system that is more suitable for the special geological environment characteristics in the upper reaches of Jinsha River. Additionally, the quantization of the vertical rainfall characteristics was optimized. Based on the research results obtained by Sun and al. (2019) [65], the Fubaopu mountain rainfall formula was used to fit the mountain rainfall in the study area. According to the prediction accuracy and landslide susceptibility map, the landslide susceptibility model established in the present study is very reasonable and can guide disaster prevention and mitigation in the upper reaches of Jinsha River.

### 5.3. Landslide Susceptibility Map Analysis

By comparing the five statistical parameters and AUC values of the three models, the RF model was determined to be the optimal model for the landslide susceptibility mapping in the study area. Therefore, the model with the highest accuracy in the five-fold cross-validation of the RF model was finally adopted in this paper to map and analyze the landslide susceptibility mapping in the study area. Furthermore, using the natural breaks method, the landslide susceptibility in the study area was divided into five grades: very low, low, moderate, high, and very high (Figure 10). The data statistics of the landslide susceptibility map (Table 6) show that the areas with very low, low, moderate, high, and very high landslide susceptibility grades are 376.08, 188.00, 125.53, 117.60, and 130.01 km<sup>2</sup>, respectively. They represented, respectively 40.13%, 20.06%, 13.39%, 12.55%, and 13.87% of the total area. The landslide areas included in the above-mentioned five susceptibility grades were 0.22, 2.20, 4.39, 15.23, and 32.94 km<sup>2</sup>, respectively. They accounted for 0.40%, 4.00%, 7.99%, 27.70%, and 59.91% of the total landslide area, respectively. According to the statistical results, the area with very high and high susceptibility accounts for 26.42% of the total area. However, it contains 87.61% of the known landslide area, indicating that this paper's landslide susceptibility maps are reasonable.

**Table 5.** Prediction accuracy of the landslide susceptibility models from different studies (ROC).

Source	Method	Conditioning Factor	Prediction Accuracy		Mapping Units
Cao et al. (2016) [23]	ICM-AHP	Slope angle, slope aspect, curvature, geology, distance to fault, distance to river, vegetation, and annual precipitation	85.74%		Grid units
Sun et al. (2018) [44]	FR	Lithology, slope angle, slope aspect, TWI, curvature, SPI, STI, topographic relief, rainfall, vegetation, NDVI, distance to river, and distance to fault	79.90%		Grid units
	AHP		76.90%		
	PCA-LR		83.40%		
Sun et al. (2020) [43]	LR	Slope angle, slope aspect, curvature, land use, NDVI, rainfall, lithology, distance to river, distance to fault, and Strahler's integral value	Training	88.16%	Slope unit (hydrological method)
			Validating	87.68%	
	ANN		Training	93.96%	
			Validating	92.60%	
	SVM		Training	89.68%	
			Validating	89.88%	
Sun et al. (2021) [49]	SVM	Lithology, slope angle, slope aspect, NDVI, land cover, rainfall, curvature, distance to river, and distance to fault	Training	89.72%	Slope unit (hydrological method)
			Validating	88.08%	
			Training	90.72%	Slope unit (curvature watershed method)
			Validating	88.96%	
This study	LR	Lithology, rock hardness, elevation, slope angle, slope aspect, topographic relief, curvature, land use, NDVI, distance from faults, Strahler's integral value, distance from rivers, rainfall, and earthquake intensity	Training	85.7%	Slope unit (curvature watershed method)
			Validating	85.2%	
	RF		Training	96.4%	
			Validating	87.0%	
	ANN		Training	91.0%	
			Validating	89.0%	

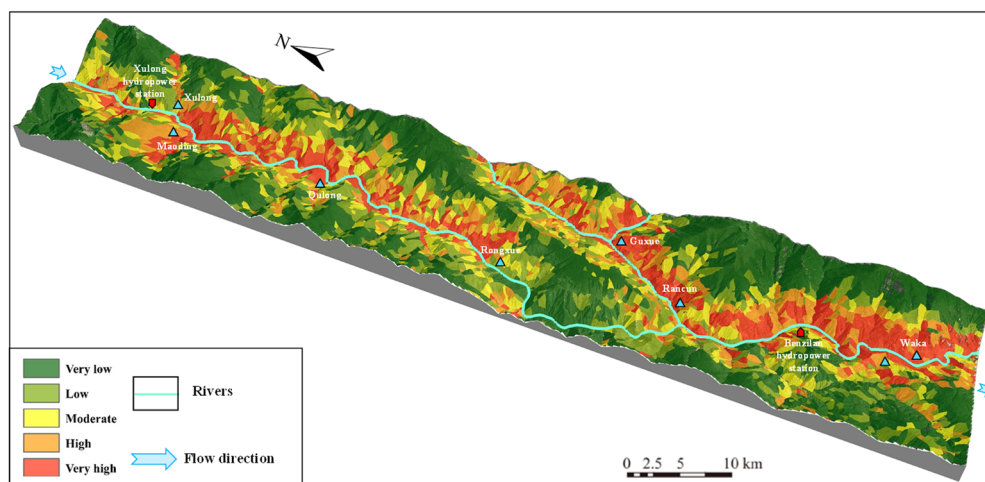


Figure 10. Landslide susceptibility map using the RF model.

Table 6. Statistical results of the landslide susceptibility map.

Susceptibility	Landslide Occurred		Total Study Area	
	Area (km <sup>2</sup> )	Ratio	Area (km <sup>2</sup> )	Ratio
Very Low	0.22	0.40%	376.08	40.13%
Low	2.20	4.00%	188.00	20.06%
Moderate	4.39	7.99%	125.53	13.39%
High	15.23	27.70%	117.60	12.55%
Very High	32.94	59.91%	130.01	13.87%

As shown in Figure 10 and Table 6, the areas with a low and very low landslide susceptibility are distributed in the medium–high elevation range. The vegetation types in this range are mainly forest, tundra, and year-round snow on the mountain top. The NDVI value in this region is large, indicating that the vegetation coverage rate in this region is high. Although the rainfall in this area is greater than that in the study area, the rainfall often occurs as snowfall at high altitudes. Additionally, this area is far away from the river and less affected, so landslides do not easily occur. The areas with moderate, high, and very high landslide susceptibilities are mainly distributed in the areas with a low elevation. In this region, the vegetation types are mainly shrubs and bare land. The NDVI value is very low, indicating that the vegetation coverage rate in this region is very low. Nearly upright soft rocks dominate the lithology in this region. It is close to rivers and faults, so it is greatly influenced by fluvial and tectonic processes. The study area is located in rapid uplift, which leads to a relatively high river erosion intensity in the study area. Under the action of rapid uplift and rapid river erosion, the bank slope becomes steeper and steeper. Many landslides will occur along the river to adapt to the action of the river and uplift. Rainfall in this area relative to the entire study area is relatively low. However, there are more landslides in this area because the entire study area’s average annual rainfall is minimal. There is a high elevation of 750 mm ±, a low elevation of only 300 mm ±, and it is very difficult for the rainfall area to achieve enough rainfall in a short amount of time to induce rainfall landslides. This is also one of the important reasons for the stable existence of many deposits in the study area. In addition, as the vertical distribution of rainfall is closely related to the distribution of vegetation, the distribution of vegetation also follows the vertical distribution law. Due to less rainfall and less vegetation in low altitude areas (a low NDVI value in low altitude areas and high NDVI value in medium–high altitude areas), the areas without vegetation coverage are more prone to landslides.

The areas with very high, high, and moderate landslide susceptibilities are mainly distributed in Guxue, Benzilan, and other villages on both sides of the Jinsha and Dingqu

Rivers. These villages have a dense population, high density of buildings, and cultivated land, and some villages have developed industries. At the same time, these villages are in the high susceptibility area of landslides, and the possibility of landslide occurrence is high. Therefore, emphasis should be placed on disaster reduction and prevention in these villages. The low and very low susceptibility areas are mainly distributed in the areas far from the Jinsha and Dingqu Rivers. Human activity in the area is relatively weak and, even if landslides occur, the damage is relatively minor.

In conclusion, the areas with a very high, high, and moderate susceptibility to landslides are mainly distributed in the areas with intensive human and engineering construction activities. Therefore, attention should be paid to disaster prevention and mitigation. Human activities are rare in areas with a low and extremely low susceptibility to landslides, and the potential threat caused by landslide disasters is minor. However, the prevention and mitigation of landslides should also be carried out in these areas. Furthermore, necessary treatment should be carried out on the high-susceptibility slope body, which affects the construction of the hydropower station.

#### *5.4. The Relationship between the Landslides and Crustal Uplift History and Glacial Age*

As can be observed from the landslide susceptibility map, landslides in the study area mostly occur along the two sides of the river, which indicates that landslides in the study area have a significant effect on the uplift of the Tibetan Plateau and glacial period. In order to determine the corresponding relationship between the landslides and the uplift stage and glacial period of the Tibetan Plateau, 27 landslides with obvious sliding surfaces in the study area were sampled by luminescence dating on their sliding surfaces. The occurrence time of each landslide in Table 7 shows that the oldest landslide is the Yahong landslide, which occurred about 118,000 years ago. A total of 5 landslides occurred in the last 10,000 years; that is, all the landslides occurred since the late Pleistocene. As can be observed from Figure 2, since the late Pleistocene, the Tibetan Plateau has entered a stage of extremely rapid uplift, during which the uplift rate of the Tibetan Plateau can reach 4.50 mm/a to 15.00 mm/a. A large number of landslides also occurred during this period, which indicates that the rapid uplift of the Tibetan Plateau has a certain correlation with the landslide occurrence. In order to understand the relationship between landslides and glacial age, this paper compares the dating data of landslides with the classification chart of the global glacial age and the classification chart of the Chinese glacial age, as shown in Figure 11. It can be observed in Figure 11 that the global glacial ages corresponding to the landslides are MIS 2 to MIS 6, and there is a good corresponding relationship. According to the classification results of the glacial ages in China, 6 landslides occurred in the late-glacial period of the Last Glacial Period, 16 landslides occurred in the Last Glacial Period, and 5 landslides occurred in the last interglacial age.

From the data, it can be observed that when the landslides occur, the Tibetan Plateau has already entered a period of rapid uplift, which would inevitably lead to the rapid downward cutting of the river. Moreover, all the landslides in the study area occurred during the last glacial and interglacial periods of the Tibetan Plateau, when the mean altitude of the Tibetan Plateau reached more than 3000 m. The moderate and long-term warm and wet airflow that moved northward greatly weakened in the Quaternary, and the dry and cold airflows that developed on a large scale in the Late Pleistocene both began during this period. During this period, the climate of the study area changed to a subtropical climate, and the three-dimensional climate in the mountains and valleys was very obvious. During the glacial period, the sea level significantly dropped due to climate change. During the Last Glacial Period, the sea level was more than 100 m lower than that of the present day, which inevitably led to the accelerated downcutting of rivers to reach the sea level of the lowest base level of erosion. Thus, the upper reaches of Jinsha River experienced rapid downcutting under the dual effects; that is, the Tibetan Plateau uplifting at a rate of 5 mm/a during this period and the rapid downcutting of the rivers due to the significant decrease in sea level. In addition, the upper Jinsha River belongs to

the plate tectonic suture zone, regionally, and the characteristic products of the DTJ in the suture zone endow the reach with a complex bank slope structure. The rapid downward cutting caused the formation of high and steep bank slopes with a height difference of over 1000 m, which provided good space and conditions for the unloading of the river valley and the continuous action of the gravity field. Additionally, the upper Jinsha River is a neotectonic active area and earthquakes are frequent. In conclusion, these basic characteristics constitute the common basic conditions for the deformation and failure of slope rock mass in the upper reaches of Jinsha River.

**Table 7.** Luminescence dating statistics of the landslides in the study area (sorted by age).

Number	Name	Method of Dating	Age (Ka)	Number	Name	Method of Dating	Age (Ka)
1	Quzhi landslide	TH	2.8 ± 0.2	15	Deze landslide	TH	42.5 ± 2.0
2	Yingui landslide	PH	3.4 ± 0.2	16	Guxue landslide	TH	45.1 ± 2.7
3	Aluogong landslide	TH	4.4 ± 0.3	17	Waka 2 landslide	TH	46.5 ± 2.1
4	Yongduo landslide	TH	5.2 ± 0.2	18	Zhanzhui landslide	TH	50.0 ± 3.1
5	Waka 1 landslide	TH	7.7 ± 0.5	19	Jinshaqiaotou landslide	TH	52.4 ± 3.0
6	Saimaoding landslide	TH	10.6 ± 0.5	20	Dari landslide	TH	56.9 ± 3.7
7	Senen landslide	TH	17.6 ± 1.1	21	Gaiyiri moraine	PH	58.8 ± 3.1
8	Maodinghe landslide	TH	18.3 ± 1.2	22	Maoding landslide	TH	70.8 ± 5.1
9	Yingui landslide	TH	19.7 ± 1.3	23	Qulong moraine	TH	77.3 ± 4.5
10	Zhisishan landslide	TH	22.7 ± 1.0	24	Yeligong moraine	TH	79.0 ± 4.1
11	Guanyinxiang landslide	TH	25.9 ± 1.6	25	Yegeding landslide	TH	81.0 ± 4.3
12	Rancun landslide	TH	31.1 ± 1.8	26	Yinduba landslide	TH	115.7 ± 7.6
13	Benzilan landslide	TH	33.2 ± 1.6	27	Yahong landslide	TH	118.1 ± 6.0
14	Waka 3 landslide	TH	41.1 ± 3.1	-	-	-	-

Notes: TH—thermoluminescence and PH—photoluminescence.

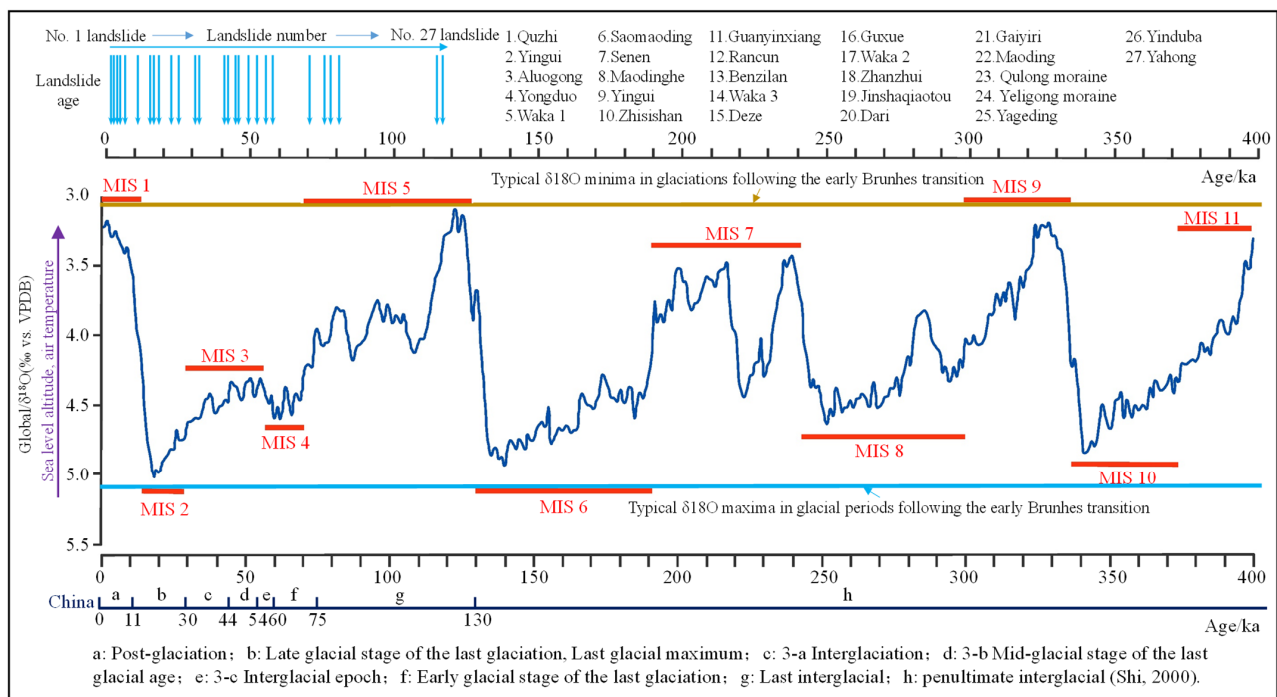


**Figure 11.** The age of the landslide in the study area corresponds to the global glacial age and the Chinese glacial age.

## 6. Conclusions

In this paper, the susceptibility of landslides under a special geodynamic system in the upper reaches of Jinsha River was mapped. First, a total of 61 landslides were mapped in the study area. Furthermore, a conditioning factors system consisting of fourteen factors was established. Then, LR, RF, and ANN models were used to build the model, and statistical parameters and ROC curves were used to optimize the model. In conclusion, the following inferences were obtained:

1. By comparing the results of the three models, it was found that the RF model is the optimal model. The area percentages of very low, low, moderate, high, and very high susceptibility classes were 40.13%, 20.06%, 13.39%, 12.55%, and 13.87%, respectively.
2. By analyzing the landslide susceptibility map, it was found that the areas with a very high, high, and moderate landslide susceptibility were mainly distributed in Guxue, Benzilan, and other villages on both sides of the Jinsha and Dingqu Rivers. Since these areas are densely populated with people and buildings, priority should be given to disaster prevention and mitigation.
3. By analyzing the relationship between landslides and crustal uplift history and glacial age, it is suggested that the landslide geological hazards in the upper reaches of Jinsha River be controlled by the double disaster effect of the geodynamic system, caused by the rapid uplift of the Tibetan Plateau and the significant decrease in sea level during the glacial period.

Some problems in the research process are also worth noting. Firstly, only Sentinel-1A data obtained in descending mode were used to interpret landslides in the study area, resulting in limitations in interpretation accuracy. Secondly, the results of susceptibility mapping are biased by ignoring the fact that topography changes after a landslide occurs. Furthermore, although the characteristics of rapid uplift were considered, the relationship between the landslide occurrence and uplift history could not be analyzed in more detail.

**Author Contributions:** Writing—original draft preparation, methodology, formal analysis, and validation, X.S.; writing—review and editing, J.C., Y.L. and N.N.R. All authors have read and agreed to the published version of the manuscript.

**Funding:** This research was funded by the National Natural Science Foundation of China (Grant No. U1702241, 41941017), and the National Key Research and Development Plan (Grant No. 2018YFC1505301).

**Institutional Review Board Statement:** Not applicable.

**Informed Consent Statement:** Not applicable.

**Data Availability Statement:** Not applicable.

**Acknowledgments:** The authors would like to thank the Editor and anonymous reviewers for their comments and suggestions, which helped to improve this paper.

**Conflicts of Interest:** The authors declare no conflict of interest.

## References

1. Broeckx, J.; Vanmaercke, M.; Duchateau, R.; Poesen, J. A data-based landslide susceptibility map of Africa. *Earth-Sci. Rev.* **2018**, *185*, 102–121. [[CrossRef](#)]
2. Deng, Q.; Fu, M.; Ren, X.; Liu, F.; Tang, H. Precedent long-term gravitational deformation of large scale landslides in the Three Gorges reservoir area, China. *Eng. Geol.* **2017**, *221*, 170–183. [[CrossRef](#)]
3. Pereira, S.; Zêzere, J.L.; Quaresma, I.D.; Bateira, C. Landslide incidence in the North of Portugal: Analysis of a historical landslide database based on press releases and technical reports. *Geomorphology* **2014**, *214*, 514–525. [[CrossRef](#)]
4. Samia, J.; Temme, A.; Bregt, A.; Wallinga, J.; Guzzetti, F.; Ardizzone, F.; Rossi, M. Do landslides follow landslides? Insights in path dependency from a multi-temporal landslide inventory. *Landslides* **2017**, *14*, 547–558. [[CrossRef](#)]
5. Wang, H.; Zhang, Y.; Hu, H. A Study on Relationship of Landslide Occurrence and Rainfall. In *Civil Engineering, Architecture and Sustainable Infrastructure II, Pts 1 and 2*; Zhao, S., Xie, Y.M., Liu, H., Gao, D., Eds.; Applied Mechanics and Materials, Trans Tech Publications Ltd.: Baech, Switzerland, 2013; Volume 438–439, pp. 1200–1204.

6. Wu, C. Landslide Susceptibility Based on Extreme Rainfall-Induced Landslide Inventories and the Following Landslide Evolution. *Water* **2019**, *11*, 2609. [[CrossRef](#)]
7. Kao, L.-S.; Chiu, Y.-H.; Tsai, C.-Y. An Evaluation Study of Urban Development Strategy Based on of Extreme Climate Conditions. *Sustainability* **2017**, *9*, 284. [[CrossRef](#)]
8. Chen, Z.; Zhou, H.; Ye, F.; Liu, B.; Fu, W. The characteristics, induced factors, and formation mechanism of the 2018 Baige landslide in Jinsha River, Southwest China. *Catena* **2021**, *203*, 105337. [[CrossRef](#)]
9. Hu, Y.-X.; Yu, Z.-Y.; Zhou, J.-W. Numerical simulation of landslide-generated waves during the 11 October 2018 Baige landslide at the Jinsha River. *Landslides* **2020**, *17*, 2317–2328. [[CrossRef](#)]
10. Tian, S.; Chen, N.; Wu, H.; Yang, C.; Zhong, Z.; Rahman, M. New insights into the occurrence of the Baige landslide along the Jinsha River in Tibet. *Landslides* **2020**, *17*, 1207–1216. [[CrossRef](#)]
11. Zhan, J.; Chen, J.; Zhang, W.; Han, X.; Sun, X.; Bao, Y. Mass movements along a rapidly uplifting river valley: An example from the upper Jinsha River, southeast margin of the Tibetan Plateau. *Environ. Earth Sci.* **2018**, *77*, 634. [[CrossRef](#)]
12. Li, Y.; Wang, C.; Dai, J.; Xu, G.; Hou, Y.; Li, X. Propagation of the deformation and growth of the Tibetan–Himalayan orogen: A review. *Earth-Sci. Rev.* **2015**, *143*, 36–61. [[CrossRef](#)]
13. Shi, Y. A Suggestion to Improve the Chronology of Quaternary Glaciations in China. *J. Glaciol. Geocryol.* **2002**, *24*, 687–692.
14. Fan, Q.; Ma, H.; Hou, G. Late Pleistocene lake and glaciation evolution on the northeastern Qinghai–Tibetan Plateau: A review. *Environ. Earth Sci.* **2011**, *66*, 625–634. [[CrossRef](#)]
15. Yi, C.; Zhu, Z.; Wei, L.; Cui, Z.; Zheng, B.; Shi, Y.; Chaolu, Y.; Zhiyong, Z.; Ling, W.; Zhijiu, C.; et al. Advances in Numerical Dating of Quaternary Glaciations in China. *Z. Geomorphol.* **2007**, *51*, 153–175. [[CrossRef](#)]
16. Wang, F.; Xu, P.; Wang, C.; Wang, N.; Jiang, N. Application of a GIS-Based Slope Unit Method for Landslide Susceptibility Mapping along the Longzi River, Southeastern Tibetan Plateau, China. *ISPRS Int. J. Geo-Inf.* **2017**, *6*, 172. [[CrossRef](#)]
17. Bao, Y.; Sun, X.; Zhou, X.; Zhang, Y.; Liu, Y. Some numerical approaches for landslide river blocking: Introduction, simulation, and discussion. *Landslides* **2021**, *18*, 3907–3922. [[CrossRef](#)]
18. Su, Y.-Q.; Gong, F.-Q.; Luo, S.; Liu, Z.-X. Experimental study on energy storage and dissipation characteristics of granite under two-dimensional compression with constant confining pressure. *J. Central South Univ.* **2021**, *28*, 848–865. [[CrossRef](#)]
19. Wu, Z.-J.; Wang, Z.-Y.; Fan, L.-F.; Weng, L.; Liu, Q.-S. Micro-failure process and failure mechanism of brittle rock under uniaxial compression using continuous real-time wave velocity measurement. *J. Central South Univ.* **2021**, *28*, 556–571. [[CrossRef](#)]
20. Dou, Z.; Tang, S.; Zhang, X.; Liu, R.; Zhuang, C.; Wang, J.; Zhou, Z.; Xiong, H. Influence of shear displacement on fluid flow and solute transport in a 3D rough fracture. *Lithosphere* **2021**, *2021*, 1569736. [[CrossRef](#)]
21. Chen, D.; Chen, H.; Zhang, W.; Lou, J.; Shan, B. An analytical solution of equivalent elastic modulus considering confining stress and its variables sensitivity analysis for fractured rock masses. *J. Rock Mech. Geotech. Eng.* **2021**; *in press*.
22. Dou, Z.; Liu, Y.; Zhang, X.; Wang, Y.; Chen, Z.; Wang, J.; Zhou, Z. Influence of Layer Transition Zone on Rainfall-Induced Instability of Multilayered Slope. *Lithosphere* **2021**, *2021*, 2277284. [[CrossRef](#)]
23. Cao, C.; Wang, Q.; Chen, J.; Ruan, Y.; Zheng, L.; Song, S.; Niu, C. Landslide Susceptibility Mapping in Vertical Distribution Law of Precipitation Area: Case of the Xulong Hydropower Station Reservoir, Southwestern China. *Water* **2016**, *8*, 270. [[CrossRef](#)]
24. Wang, Z.; Cui, P.; Yu, G.-A.; Zhang, K. Stability of landslide dams and development of knickpoints. *Environ. Earth Sci.* **2012**, *65*, 1067–1080. [[CrossRef](#)]
25. Wang, P.; Chen, J.; Dai, F.; Long, W.; Xu, C.; Sun, J.; Cui, Z. Chronology of relict lake deposits around the Suwalong paleolandslide in the upper Jinsha River, SE Tibetan Plateau: Implications to Holocene tectonic perturbations. *Geomorphology* **2014**, *217*, 193–203. [[CrossRef](#)]
26. Ning, Y.; Zhang, G.; Tang, H.; Shen, W.; Shen, P. Process Analysis of Toppling Failure on Anti-dip Rock Slopes Under Seismic Load in Southwest China. *Rock Mech. Rock Eng.* **2019**, *52*, 4439–4455. [[CrossRef](#)]
27. Tao, Z.; Zhu, C.; He, M.; Karakus, M. A physical modeling-based study on the control mechanisms of Negative Poisson's ratio anchor cable on the stratified toppling deformation of anti-inclined slopes. *Int. J. Rock Mech. Min. Sci.* **2021**, *138*, 104632. [[CrossRef](#)]
28. Wang, Y.; Yang, H.; Han, J.; Zhu, C. Effect of rock bridge length on fracture and damage modelling in granite containing hole and fissures under cyclic uniaxial increasing-amplitude decreasing-frequency (CUIADF) loads. *Int. J. Fatigue* **2022**, *158*, 106741. [[CrossRef](#)]
29. Zhang, G.; Wang, F.; Zhang, H.; Tang, H.; Li, X.; Zhong, Y. New stability calculation method for rock slopes subject to flexural toppling failure. *Int. J. Rock Mech. Min. Sci.* **2018**, *106*, 319–328. [[CrossRef](#)]
30. Zhu, C.; He, M.; Karakus, M.; Cui, X.; Tao, Z. Investigating Toppling Failure Mechanism of Anti-dip Layered Slope due to Excavation by Physical Modelling. *Rock Mech. Rock Eng.* **2020**, *53*, 5029–5050. [[CrossRef](#)]
31. Zhu, C.; Karakus, M.; He, M.; Meng, Q.; Shang, J.; Wang, Y.; Yin, Q. Volumetric deformation and damage evolution of Tibet interbedded skarn under multistage constant-amplitude-cyclic loading. *Int. J. Rock Mech. Min. Sci.* **2022**, *152*, 105066. [[CrossRef](#)]
32. Zhang, Y.; Tang, H.; Li, C.; Lu, G.; Cai, Y.; Zhang, J.; Tan, F. Design and Testing of a Flexible Inclinator Probe for Model Tests of Landslide Deep Displacement Measurement. *Sensors* **2018**, *18*, 224. [[CrossRef](#)]
33. Su, M.-B.; Chen, I.-H.; Liao, C.-H. Using TDR Cables and GPS for Landslide Monitoring in High Mountain Area. *J. Geotech. Geoenviron. Eng.* **2009**, *135*, 1113–1121. [[CrossRef](#)]

34. Zhu, H.-H.; Shi, B.; Zhang, C.-C. FBG-Based Monitoring of Geohazards: Current Status and Trends. *Sensors* **2017**, *17*, 452. [[CrossRef](#)] [[PubMed](#)]
35. Cavièdes-Voullième, D.; Juez, C.; Murillo, J.; García-Navarro, P. 2D dry granular free-surface flow over complex topography with obstacles. Part I: Experimental study using a consumer-grade RGB-D sensor. *Comput. Geosci.* **2014**, *73*, 177–197. [[CrossRef](#)]
36. Cao, C.; Zhang, W.; Chen, J.; Shan, B.; Song, S.; Zhan, J. Quantitative estimation of debris flow source materials by integrating multi-source data: A case study. *Eng. Geol.* **2021**, *291*, 106222. [[CrossRef](#)]
37. Wasowski, J.; Bovenga, F. Investigating landslides and unstable slopes with satellite Multi Temporal Interferometry: Current issues and future perspectives. *Eng. Geol.* **2014**, *174*, 103–138. [[CrossRef](#)]
38. Yang, W.; Liu, L.; Shi, P. Detecting precursors of an imminent landslide along the Jinsha River. *Nat. Hazards Earth Syst. Sci.* **2020**, *20*, 3215–3224. [[CrossRef](#)]
39. Zhao, C.; Kang, Y.; Zhang, Q.; Lu, Z.; Li, B. Landslide Identification and Monitoring along the Jinsha River Catchment (Wudongde Reservoir Area), China, Using the InSAR Method. *Remote Sens.* **2018**, *10*, 993. [[CrossRef](#)]
40. Pham, B.T.; Bui, D.T.; Pourghasemi, H.R.; Indra, P.; Dholakia, M.B. Landslide susceptibility assessment in the Uttarakhand area (India) using GIS: A comparison study of prediction capability of naïve bayes, multilayer perceptron neural networks, and functional trees methods. *Arch. Meteorol. Geophys. Bioclimatol. Ser. B* **2017**, *128*, 255–273. [[CrossRef](#)]
41. Pham, B.T.; Bui, D.T.; Dholakia, M.; Prakash, I.; Pham, H.V.; Mehmood, K.; Le, H.Q. A novel ensemble classifier of rotation forest and Naïve Bayer for landslide susceptibility assessment at the Luc Yen district, Yen Bai Province (Viet Nam) using GIS. *Geomat. Nat. Hazards Risk* **2017**, *8*, 649–671. [[CrossRef](#)]
42. Pradhan, B.; Lee, S. Landslide susceptibility assessment and factor effect analysis: Backpropagation artificial neural networks and their comparison with frequency ratio and bivariate logistic regression modelling. *Environ. Model. Softw.* **2010**, *25*, 747–759. [[CrossRef](#)]
43. Sun, X.; Chen, J.; Han, X.; Bao, Y.; Zhan, J.; Peng, W. Application of a GIS-based slope unit method for landslide susceptibility mapping along the rapidly uplifting section of the upper Jinsha River, South-Western China. *Bull. Eng. Geol. Environ.* **2020**, *79*, 533–549. [[CrossRef](#)]
44. Sun, X.; Chen, J.; Bao, Y.; Han, X.; Zhan, J.; Peng, W. Landslide Susceptibility Mapping Using Logistic Regression Analysis along the Jinsha River and Its Tributaries Close to Derong and Deqin County, Southwestern China. *ISPRS Int. J. Geo-Inf.* **2018**, *7*, 438. [[CrossRef](#)]
45. Harris, N. The elevation history of the Tibetan Plateau and its implications for the Asian monsoon. *Palaeogeogr. Palaeoclim. Palaeoecol.* **2006**, *241*, 4–15. [[CrossRef](#)]
46. Li, J.; Fang, X. Uplift of the Tibetan Plateau and environmental changes. *Chin. Sci. Bull.* **1999**, *44*, 2117–2124. [[CrossRef](#)]
47. Xiao, X.C.; Wang, J. A brief review of tectonic evolution and uplift of the Qinghai-Tibet Plateau. *Geol. Rev.* **1998**, *44*, 372–381.
48. Chen, J.; Li, H. Genetic Mechanism and Disasters Features of Complicated Structural Rock Mass Along the Rapidly Uplift Section at the Upstream of Jinsha River. *J. Jilin Univ.* **2016**, *46*, 1153–1167.
49. Sun, X.; Chen, J.; Han, X.; Bao, Y.; Zhou, X.; Peng, W. Landslide susceptibility mapping along the upper Jinsha River, south-western China: A comparison of hydrological and curvature watershed methods for slope unit classification. *Bull. Eng. Geol. Environ.* **2020**, *79*, 4657–4670. [[CrossRef](#)]
50. Ba, Q.; Chen, Y.; Deng, S.; Yang, J.; Li, H. A comparison of slope units and grid cells as mapping units for landslide susceptibility assessment. *Earth Sci. Inform.* **2018**, *11*, 373–388. [[CrossRef](#)]
51. Broeckx, J.; Maertens, M.; Isabirye, M.; Vanmaercke, M.; Namazzi, B.; Deckers, J.; Tamale, J.; Jacobs, L.; Thiery, W.; Kervyn, M.; et al. Landslide susceptibility and mobilization rates in the Mount Elgon region, Uganda. *Landslides* **2019**, *16*, 571–584. [[CrossRef](#)]
52. Dhianaufal, D.; Kristyanto, T.H.W.; Indra, T.L.; Syahputra, R. Fuzzy Logic Method for Landslide Susceptibility Mapping in Volcanic Sediment Area in Western Bogor. In Proceedings of the 3rd International Symposium on Current Progress in Mathematics and Sciences, Bali, Indonesia, 26–27 July 2017.
53. Lee, C.-T.; Chung, C.-C. Common Patterns among Different Landslide Susceptibility Models of the Same Region. In *Advancing Culture of Living with Landslides. Volume 2: Advances in Landslide Science, Proceedings of the 4th World Landslide Forum, Ljubljana, Slovenia, 29 May–2 June 2017*; Springer International Publishing: Cham, Switzerland, 2017; pp. 937–942.
54. Xing, X.; Wu, C.; Li, J.; Li, X.; Zhang, L.; He, R. Susceptibility assessment for rainfall-induced landslides using a revised logistic regression method. *Nat. Hazards* **2021**, *106*, 97–117. [[CrossRef](#)]
55. Guzzetti, F.; Mondini, A.C.; Cardinali, M.; Fiorucci, F.; Santangelo, M.; Chang, K.-T. Landslide inventory maps: New tools for an old problem. *Earth-Sci. Rev.* **2012**, *112*, 42–66. [[CrossRef](#)]
56. Dai, K.; Li, Z.; Tomás, R.; Liu, G.; Yu, B.; Wang, X.; Cheng, H.; Chen, J.; Stockamp, J. Monitoring activity at the Daguangbao mega-landslide (China) using Sentinel-1 TOPS time series interferometry. *Remote Sens. Environ.* **2016**, *186*, 501–513. [[CrossRef](#)]
57. Fárová, K.; Jelének, J.; Kopačková-Strnadová, V.; Kysel, P. Comparing DInSAR and PSI Techniques Employed to Sentinel-1 Data to Monitor Highway Stability: A Case Study of a Massive Dobkovičky Landslide, Czech Republic. *Remote Sens.* **2019**, *11*, 2670. [[CrossRef](#)]
58. Du, Q.; Li, G.; Zhou, Y.; Chai, M.; Chen, D.; Qi, S.; Wu, G. Deformation Monitoring in an Alpine Mining Area in the Tianshan Mountains Based on SBAS-InSAR Technology. *Adv. Mater. Sci. Eng.* **2021**, *2021*, 9988017. [[CrossRef](#)]

59. Jiang, C.; Fan, W.; Yu, N.; Nan, Y. A New Method to Predict Gully Head Erosion in the Loess Plateau of China Based on SBAS-InSAR. *Remote Sens.* **2021**, *13*, 421. [[CrossRef](#)]
60. Steger, S.; Mair, V.; Kofler, C.; Pittore, M.; Zebisch, M.; Schneiderbauer, S. Correlation does not imply geomorphic causation in data-driven landslide susceptibility modelling—Benefits of exploring landslide data collection effects. *Sci. Total Environ.* **2021**, *776*, 145935. [[CrossRef](#)] [[PubMed](#)]
61. Lombardo, L.; Tanyas, H.; Nicu, I.C. Spatial modeling of multi-hazard threat to cultural heritage sites. *Eng. Geol.* **2020**, *277*, 105776. [[CrossRef](#)]
62. Wang, K.; Zhang, S.; Wei, F. Slope Unit Extraction Methods: Advances and Prospects. *J. Yangtze River Sci. Res. Inst.* **2020**, *37*, 85–93.
63. Alvioli, M.; Marchesini, I.; Reichenbach, P.; Rossi, M.; Ardizzone, F.; Fiorucci, F.; Guzzetti, F. Automatic delineation of geomorphological slope units with r.slopeunits v1.0 and their optimization for landslide susceptibility modeling. *Geosci. Model Dev.* **2016**, *9*, 3975–3991. [[CrossRef](#)]
64. Pourghasemi, H.R.; Rossi, M. Landslide susceptibility modeling in a landslide prone area in Mazandarn Province, north of Iran: A comparison between GLM, GAM, MARS, and M-AHP methods. *Arch. Meteorol. Geophys. Bioclimatol. Ser. B* **2017**, *130*, 609–633. [[CrossRef](#)]
65. Sun, X.; Chen, J.; Bao, Y.; Han, X.; Zhan, J.; Peng, W. Flash flood schlep ability estimation in vertical distribution law of the precipitation area: A case of Xulong gully, Southwest China. *Arab. J. Geosci.* **2019**, *12*, 279. [[CrossRef](#)]
66. Lai, M.; Zhu, J.G.; Jiang, P.; Sun, Z.T.; Da-Hu, L.I.; Hua, Y.U.; Long, C.H.; Zhu, Y.L. Ground motion data study of the 2013 Deqing-Derong M5. 9 Earthquake. *Earthq. Res. Sichuan* **2014**. [[CrossRef](#)]
67. Budimir, M.E.A.; Atkinson, P.M.; Lewis, H.G. A systematic review of landslide probability mapping using logistic regression. *Landslides* **2015**, *12*, 419–436. [[CrossRef](#)]
68. Chen, Z.; Wang, J. Landslide hazard mapping using logistic regression model in Mackenzie Valley, Canada. *Nat. Hazards* **2007**, *42*, 75–89. [[CrossRef](#)]
69. Lee, S.; Sambath, T. Landslide susceptibility mapping in the Damrei Romel area, Cambodia using frequency ratio and logistic regression models. *Environ. Earth Sci.* **2006**, *50*, 847–855. [[CrossRef](#)]
70. Solaimani, K.; Mousavi, S.Z.; Kavian, A. Landslide susceptibility mapping based on frequency ratio and logistic regression models. *Arab. J. Geosci.* **2012**, *6*, 2557–2569. [[CrossRef](#)]
71. Breiman, L. Random forests. *Mach. Learn.* **2001**, *45*, 5–32. [[CrossRef](#)]
72. Hong, H.; Miao, Y.; Liu, J.; Zhu, A.-X. Exploring the effects of the design and quantity of absence data on the performance of random forest-based landslide susceptibility mapping. *Catena* **2019**, *176*, 45–64. [[CrossRef](#)]
73. Kim, J.-C.; Lee, S.; Jung, H.-S.; Lee, S. Landslide susceptibility mapping using random forest and boosted tree models in Pyeong-Chang, Korea. *Geocarto Int.* **2018**, *33*, 1000–1015. [[CrossRef](#)]
74. Miao, T.Y.; Wang, M. Susceptibility Analysis of Earthquake-Induced Landslide Using Random Forest Method. In Proceedings of the International Conference on Computer Information Systems and Industrial Applications, Bangkok, Thailand, 28–29 June 2015.
75. Sun, D.; Wen, H.; Wang, D.; Xu, J. A random forest model of landslide susceptibility mapping based on hyperparameter optimization using Bayes algorithm. *Geomorphology* **2020**, *362*, 107201. [[CrossRef](#)]
76. Polykretis, C.; Chalkias, C. Comparison and evaluation of landslide susceptibility maps obtained from weight of evidence, logistic regression, and artificial neural network models. *Nat. Hazards* **2018**, *93*, 249–274. [[CrossRef](#)]
77. Poudyal, C.P.; Chang, C.; Oh, H.-J.; Lee, S. Landslide susceptibility maps comparing frequency ratio and artificial neural networks: A case study from the Nepal Himalaya. *Environ. Earth Sci.* **2010**, *61*, 1049–1064. [[CrossRef](#)]
78. Saro, L.; Woo, J.S.; Kwan-Young, O.; Moun-Jin, L. The spatial prediction of landslide susceptibility applying artificial neural network and logistic regression models: A case study of Inje, Korea. *Open Geosci.* **2016**, *8*, 117–132. [[CrossRef](#)]
79. Bao, Y.; Zhai, S.; Chen, J.; Xu, P.; Sun, X.; Zhan, J.; Zhang, W.; Zhou, X. The evolution of the Samaoding paleolandslide river blocking event at the upstream reaches of the Jinsha River, Tibetan Plateau. *Geomorphology* **2020**, *351*, 106970. [[CrossRef](#)]
80. Yu, C.; Chen, J. Application of a GIS-Based Slope Unit Method for Landslide Susceptibility Mapping in Helong City: Comparative Assessment of ICM, AHP, and RF Model. *Symmetry* **2020**, *12*, 1848. [[CrossRef](#)]
81. Su, Q.; Zhang, J.; Zhao, S.; Wang, L.; Liu, J.; Guo, J. Comparative Assessment of Three Nonlinear Approaches for Landslide Susceptibility Mapping in a Coal Mine Area. *ISPRS Int. J. Geo-Inf.* **2017**, *6*, 228. [[CrossRef](#)]